Antiferromagnetism, ferromagnetism, and magnetic phase separation in $Bi_2Sr_2CoO_{6+\delta}$

K. J. Thomas, Y. S. Lee, F. C. Chou, B. Khaykovich, P. A. Lee, and M. A. Kastner

Department of Physics and Center for Material Science and Engineering, Massachusetts Institute of Technology,
Cambridge, Massachusetts 02139

R. J. Cava

Department of Chemistry, Princeton University, Princeton, New Jersy 08544

J. W. Lynn

NIST Center for Neutron Research, Gaithersburg, Maryland 20899-8562

We present results of a study of the magnetism in $Bi_2Sr_2CoO_{6+\delta}$, the Co analog of the high T_c superconductor $Bi_2Sr_2CuO_{6+\delta}$. This system evolves from an antiferromagnetic (AF) insulator to an unusual ferromagnetic (FM) insulator as δ is reduced from ~ 0.5 to ~ 0.25. When δ is close to 0.5, the Co ions have formal oxidation state 3+ and order antiferromagnetically at $T_N \sim 250$ K. The $\delta \sim 0.25$ crystal has equal numbers of Co^{2+} and Co^{3+} and exhibits FM behavior with a moment $\sim 1.5 \mu_b$/Co at 5 T and a Curie temperature $T_c \sim 100$ K. Single crystal neutron scattering (both polarized and unpolarized), magnetization, and resistivity measurements have been used to characterize the evolution of the magnetic and transport properties between these two doping limits. For crystals with $0.25 < \delta < 0.5$, both FM and AF Bragg peaks are observed with neutrons, above a critical field H_c. Field-dependent neutron diffraction measurements confirm that the FM peaks result from ferromagnetic domains, which coexist with antiferromagnetic domains, and have a net moment above the critical field. The suppression of Néel order and accompanying increase in the volume of the FM domains with decreasing δ is measured for samples with $0.25 < \delta < 0.5$. We discuss this behavior in the context of phase separation resulting in a hole rich, Co^{3+} AF phase and a hole poor, Co^{2+}–Co^{3+} FM phase. In addition, the rich phenomenology of the interacting magnetic domains can be explained by mapping to a form of the random field Ising model.

PACS number(s): 75.25.+z

I. INTRODUCTION

In many transition metal oxides, the delicate interplay between the charge, orbital, and spin degrees of freedom results in a rich phase diagram. For example, the manganites, of general form $A_{1-x}B_xMnO_3$ (A is a rare earth, and B is a divalent alkali earth atom), show a complex evolution of the magnetic and transport properties with hole doping.[1–3] Charge ordering, ferromagnetic (FM), and antiferromagnetic (AF) ordering, and a transition from metallic to insulating behavior are all observed in the range $0 < x < 1$. The phase diagram as a function of x depends on the choice of A and B ions, but the general feature of the manganites is that hole doping of the pure Mn^{3+} insulator results in ferromagnetism accompanied by large magnetoresistance (MR). Although the existence of FM order at finite x is qualitatively explained by double-exchange (DE) between the Mn^{3+} and Mn^{4+} ions, it has become clear that a more complete physical picture is required to explain all of the experimental observations.

To gain insight into the physics of the manganites, the magnetic and electronic properties of related compounds have been studied intensively. The cobalt oxides, in particular, have attracted attention both because they exhibit similar properties to the manganites and because they constitute an interesting group of materials in their own right. The formal oxidation state of Co can be 2+, 3+ or 4+ with the result that a wide range of mixed valence compounds can be obtained with chemical substitution. In addition, the crystal field splitting and on-site exchange (Hund's rule) are in close competition for the Co ion, resulting in the possibility for temperature driven spin-state transitions and a high sensitivity to changes in the local ligand field.[4] This is an important difference between the Co compounds and the manganites, since the Mn ions in the manganites are always in the high spin state. Finally, there are several examples of cobalt-oxides that are readily doped with oxygen such that the hole concentration can be varied in a single sample.[5,6]

The discovery of MR in thin films of $La_{1-x}Sr_xCoO_3$ has directed considerable attention to this compound.[7] In bulk $La_{1-x}Sr_xCoO_3$, the introduction of Co^{4+} with increasing x results in a FM transition and MR, although the MR is substantially smaller than that seen in the manganites. MR is also observed in the perovskite based compound $RBaCo_2O_5$ ($R=$Eu, Gd).[8] These materials exhibit a number of electronic and magnetic phases because they accommodate δ at several nonstoichiometric values between 0 and 1. For example, the $YBaCo_2O_5$ compound ($\delta=0$) exhibits charge order of the Co^{3+} and Co^{2+} ions.[6,9] Charge ordering has also been observed in $La_{1.5}Sr_{0.5}CoO_4$ where Co^{2+} and Co^{3+} are in the ratio of 1:1.[10]

Although one of the major themes in the study of the manganites is the role of phase separation,[1,11] there appears to be little evidence for phase separation occurring in the cobalt-oxides. One exception may be $La_{1-x}Sr_xCoO_3$, where recent susceptibility and electron diffraction results suggest electronic phase separation.[12–14] In $La_{1-x}Sr_xCoO_3$, hole-rich

FM clusters form near the Sr ions and leave behind a hole poor matrix with La_2CoO_3 character.

The formation of distinct phases with different hole densities is limited by long range Coulomb interactions. However, when compounds are doped with oxygen, electronic phase separation may be accommodated by the mobility of oxygen. In this paper, we report on our observation of magnetic phase separation in oxygen doped $Bi_2Sr_2CoO_{6+\delta}$ in the range $0.25 < \delta < 0.5$. We show neutron scattering results that suggest phase separation between a Co^{3+} rich AF phase and a Co^{2+}–Co^{3+} FM phase. The phase separation occurs on sufficiently small length scales that the magnetic interaction at the phase boundary has a non-negligible effect on the magnetic order within the individual phases. In addition, we believe that the mobility of oxygen accommodates the formation of distinct phases with different hole densities.

Tarascon and co-workers[15] first synthesized $Bi_2Sr_2CoO_{6+\delta}$ in an effort to study the effects of replacing Cu with Co in the high-T_c superconductor $Bi_2Sr_2CuO_{6+\delta}$. They found that the Co compound is essentially isostructural to the cuprate with the exception that the structural modulation along the orthorhombic a-axis has a period of four lattice constants instead of five.

The Co spins in powder samples of $Bi_2Sr_2CoO_{6+\delta}$ were found to order antiferromagnetically in the ab plane at a Néel temperature T_N between 100 and 280 K, depending on sample preparation, yet the susceptibility along **a** showed a FM peak at T_N. Below T_N, the field dependence of the moment along **a** was superlinear, suggesting hidden ferromagnetism. The authors of Ref. 15 suggested that an in-plane canting of the antiferromagnetic spins could explain the ferromagnetic behavior. However, this was based on their observation that the AF spin lies along the **b** direction, perpendicular to the observed FM jump in the moment. Our measurements of single crystal $Bi_2Sr_2CoO_{6+\delta}$ show that the spin direction is, instead, along **a**, which excludes the simple canting model described in Ref. 15.[16]

Here, we report an extensive investigation of the FM behavior of $Bi_2Sr_2CoO_{6+\delta}$, focusing, in particular, on the enhancement of the ferromagnetism as the oxygen content, δ, is decreased from $\delta > 0.4$ to $\delta \sim 0.25$. We show evidence that the FM susceptibility and field induced uniform moment result from FM clusters within the antiferromagnet. The clusters grow larger when oxygen is removed from the crystal and dominate the magnetic behavior in samples in which T_N is reduced below ~ 100 K. To understand the evolution of the FM clusters with the removal of oxygen, we have characterized crystals with $0.25 \lesssim \delta < 0.5$. We find that the oxygen-rich crystal ($\delta > 0.4$) with mostly Co^{3+} shows AF long-range order.[17] When the oxygen content δ is close to 0.25, such that the ratio of Co^{3+} to Co^{2+} approaches 1:1, the spins order ferromagnetically along **a**. At intermediate values of δ, $0.25 < \delta < 0.5$, we observe both AF and FM domains with neutrons. We argue that phase separation into domains which are hole rich (mostly Co^{3+}) and domains which are hole poor (equal numbers of Co^{2+} and Co^{3+}) results in distinct magnetic domains which are AF and FM, respectively. Phase separation into hole rich and hole poor regions at high temperatures is presumably allowed by mobile oxygen, for

which an imiscibility gap between the $\delta = 0.5$ and $\delta = 0.25$ compositions may exist. In addition, we suggest that the FM phase is a charge-ordered checkerboard structure with alternating Co^{3+} and Co^{2+} ions.

Our paper is organized as follows. In Sec. II, the sample preparation and characterization of single crystal $Bi_2Sr_2CoO_{6+\delta}$ are discussed. The results are presented in three parts in Sec. III. In Sec. III A, we discuss the antiferromagnetic spin arrangement for the composition with $\delta > 0.4$, which consists of predominantly Co^{3+} ions. In Sec. III B, we present evidence for ferromagnetic order near the limit $\delta \sim 0.25$. This oxygen concentration should correspond to nearly equal amounts of Co^{2+} and Co^{3+} ions and is apparently the optimal concentration for forming the FM phase. In Sec. III C, we discuss the presence of simultaneous FM and AF order, which exists in all samples with $0.25 < \delta < 0.5$. Neutron scattering and magnetization measurements of samples with a range of T_N from 295 to 0 K are presented to show the evolution of the FM clusters as oxygen vacancies are introduced into the Co^{3+} AF. Presenting the data in this way clarifies which properties are intrinsic to either the FM phase or the AF phase and which properties result from the coexistence and interaction of two distinct magnetic phases at intermediate δ. In Sec. IV, we discuss the experimental results in terms of phase separation between the Co^{3+} AF and the Co^{2+}–Co^{3+} charge ordered FM. We present a microscopic model to explain the field dependence observed in the magnetically ordered, phase separated crystal and show that this model can be mapped to a form of the random field Ising model in two dimensions.

II. EXPERIMENTAL DETAILS

Single crystals of $Bi_2Sr_2CoO_{6+\delta}$ were grown by the traveling solvent floating zone method. The polycrystalline stoichiometric feed rod was prepared from a solid state reaction of Bi_2O_3, $SrCO_3$, and Co_3O_4 powders and the mixed powder was calcined at $850\,°C$ for 12 h followed by a second anneal at $890\,°C$ for 12 h. The final feed rod was annealed at $900\,°C$ in air. A Bi_2O_3 rich flux was chosen at a molar ratio of 4:1 $Bi_2Sr_2CoO_6$ to Bi_2O_3. X-ray diffraction of crushed crystals confirmed that the crystals consist of a single chemical phase. As-grown samples typically have $T_N \gtrsim 200$ K.

Figure 1 shows the crystal structure of $Bi_2Sr_2CoO_{6+\delta}$. For clarity, the modulation along **a**, which results in a fourfold increase of the unit cell, is not shown. Note that each Co site in $Bi_2Sr_2CoO_{6+\delta}$ is surrounded by six oxygen ions in an elongated octahedron and in the absence of the long-wavelength modulation, the Co sites would form a nearly square lattice in the CoO_2 layers. Throughout this paper, we use notation describing the orthorhombic subcell of $Bi_2Sr_2CoO_{6+\delta}$ with lattice parameters $a \simeq b \simeq 5.45$ Å and $c \simeq 23.6$ Å.

The crystal grows along **b** and cleaves easily into rectangular pieces with the long axis along **b** and the large faces perpendicular to **c**. X-ray Laue diffraction confirms the superlattice reflections along **a**. These features are used to orient small rectangular pieces to within $3°$ degrees of one of the major crystallographic axes for magnetization measure-
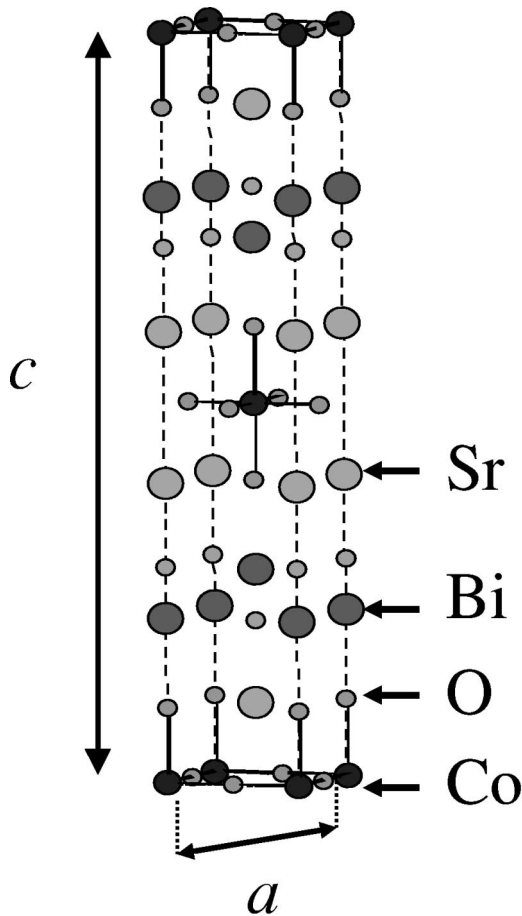
FIG. 1. Structure of the tetragonal subcell in $Bi_2Sr_2CoO_{6+\delta}$, indicating the orthorhombic a-axis. The modulation along **a** is not shown. Each Co ion is surrounded by an elongated octahedron of oxygen ions.

ments. Large, single crystal cylindrical rods, of order 3–5 mm in diameter and 3 cm in length, are used for neutron scattering measurements. For most of the samples, magnetometry measurements are made on a small piece cut from the same crystal used for neutron diffraction and provide an important check on the magnetic moments calculated from neutron measurements.

The magnetic properties of $Bi_2Sr_2CoO_{6+\delta}$ are very sensitive to the oxygen content, which, in turn, is determined by the annealing conditions. Annealing an as-grown crystal in vacuum reduces the Néel temperature, T_N, significantly. For example, annealing at $600\,°C$ in vacuum ($\leqslant 10$ mTorr) for 2 h reduces T_N from 235 to 170 K. For annealing temperatures between 400 and $850\,°C$, the higher the temperature of the vacuum anneal, the lower the resulting T_N. In addition, the structural model used in the refinement of the neutron powder diffraction data from Ref. 15 includes an extra row of oxygen in the bismuth–oxide layer, consistent with a formula unit of $Bi_2Sr_2CoO_{6.25}$. These two points suggest that the as-grown crystals have $\delta > 0.25$, which favors trivalent Co. One expects an AF interaction between neighboring Co^{3+} ions with nonzero spin, S. Thus, the suppression of AF order when oxygen is removed indicates that the composition with all cobalt ions in the high oxidation, or 3+ state,

would have an antiferromagnetic state with the highest T_N.

Several groups have measured the oxygen content either directly [thermogravimetric analysis (TGA)] or indirectly (titration of the Co^{3+}) for as-grown crystals.[15,18] The results vary substantially, from $\delta = 0.15$ (titration) (Ref. 15) to $\delta = 0.4$ (TGA).[15,18] In the TGA method, a sample of $Bi_2Sr_2CoO_{6+\delta}$ is annealed at high temperature in a reducing atmosphere until the crystal decomposes into Bi and Co metals and SrO. The weight loss during decomposition is equated to the loss of $(4+\delta)$ oxygen atoms per formula unit. This method has been used to estimate the oxygen content of our as-grown samples. A flow of 5% H_2 in He gas provides a reducing environment for a single crystal (2–20 mg) with initial $T_N = 260$ K. For several such TGA measurements in which the sample is decomposed, the range of δ measured is $0.23 \leqslant \delta \leqslant 0.5$. The error in this measurement results primarily from incomplete decomposition and the partial evaporation of Bi.

Although there is a large uncertainty in the *absolute* oxygen content of the most oxygenated crystal, the *difference* in oxygen content between two samples which have different Néel temperatures can be measured very accurately. We first anneal a crystal in vacuum so that the AF ordering is completely suppressed. Since, as mentioned above, the structural oxygen content is $\delta = 0.25$, it is not unreasonable to assume that this reduced crystal is close to the composition $\delta = 0.25$. We then measure the weight gain after annealing the crystal at $560\,°C$ in oxygen in the TGA. The reoxidized crystal has a T_N of 240 K and 0.16 more oxygen per formula unit than the reduced crystal. Therefore, we determine that a crystal with $T_N = 240$ K has $\delta = 0.41$, in good agreement with the value of $\delta = 0.37$ for as-grown crystals determined by Zinkevich *et al.*[18] Samples with δ greater than 0.4 can be obtained by further annealing in oxygen at temperatures $> 560\,°C$. Annealing at $800\,°C$ in oxygen results in a T_N as high as 295 K; however, this is also the temperature at which $Bi_2Sr_2CoO_{6+\delta}$ becomes unstable to formation of the double-layer compound $Bi_2Sr_3Co_2O_{9+\delta}$ and the oxidation of $Bi_2Sr_2CoO_{6+\delta}$ is therefore limited.[18] From the above, we can say that samples with $T_N > 240$ K have $\delta > 0.4$, though we do not believe we have reached the composition $\delta = 0.5$ corresponding to only Co^{3+}.

To obtain samples for neutron scattering and magnetization measurements with $T_N < 200$ K, as-grown crystals were annealed in vacuum for up to 12 h. To obtain the most reduced samples, as-grown crystals were annealed at $800\,°C$ in an evacuated quartz tube containing Cu powder as a reducing agent. Although this procedure resulted in the most complete reduction of the sample (no measurable Co^{3+} AF), the large temperature gradients in this process warped the weakly coupled layers and samples obtained in this way had poor mosaics consisting of several crystallites.

Single crystal neutron scattering measurements were made at the BT2 triple-axis spectrometer at NIST. Samples that were reduced in the quartz tube contained multiple crystallites and, in this case, the largest crystallite was chosen for neutron study. The crystal mosaic varied, depending on the

sample, from 0.1° to 1°. Different collimator slit widths (FWHM) were chosen depending on the sample mosaic, although most measurements were taken using 60′ - 40′ - sample - 40′ beam collimation with no collimator before the detector. Field-dependent measurements were made using a split-coil superconducting magnet in conjunction with a He cryostat. The incident neutron energy was 14.7 meV. For the unpolarized neutron measurements, the (0, 0, 2) reflection from pyrolytic graphite (PG) crystals was used for the monochromator and analyzer. For the polarized neutron measurements, a Heusler alloy was used for the monochromator and either a PG was used for the analyzer (half-polarization analysis) or another Heusler was used (full-polarization analysis). The flipping ratio in the polarization measurements exceeded 20:1, indicating that more than 95% of the neutrons remained polarized over the course of the scattering flight path. We calculated the magnetic moment per Co ion (in absolute units) by comparing the intensities of the magnetic peaks to those of the nuclear peaks. In these calculations, we used the structure factors calculated in the powder refinement from Ref.15. All graphs showing raw neutron data show statistical error bars, though in some cases, the error bar is smaller than the plot symbol. Unless otherwise noted, the measured magnetic Bragg peaks were resolution limited in width.

The temperature dependent magnetic susceptibility, $\chi(T)$, and field-dependent uniform moment were measured in a Superconducting QUantum Interference Device (SQUID) magnetometer over the temperature range 5–400 K. Transport measurements were made on cleaved rectangular pieces with a thickness of 100–200 μm. Line contacts of Cr and then Au were evaporated onto the top and sides for voltage and current contacts, respectively. Au wire leads were attached using silver epoxy cured at 100 °C in air. Contacts applied in this way resulted in room temperature contact resistances of 0.1–2 kΩ.

III. RESULTS

A. Antiferromagnetic order in $Bi_2Sr_2CoO_{6+\delta}$, $\delta \gtrsim 0.4$

In this section, we discuss the details of the antiferromagnetic order of the Co^{3+} spins occurring in samples with $\delta \gtrsim 0.4$. Initial neutron scattering measurements of the spin ordering in as-grown crystals were performed at zero field in both the (H0L) and (0KL) scattering planes. We determined $T_N \sim 235$ K from the peak in the susceptibility, as discussed below. The neutron measurements revealed magnetic Bragg peaks at the positions (H = odd, K = even, L = odd) and (H = even, K = odd, L = even), consistent with antiparallel nearest-neighbor (NN) spins in the CoO_2 layer and an effective FM interaction between NN spins in adjacent layers, as shown in Fig. 2(a).[19] The four unique spins in the magnetic unit cell are therefore at the positions (0, 0, 0), (1/2, 1/2, 0), (1/2, 0, 1/2), and (0, 1/2, 1/2). Figure 2(b) summarizes the allowed nuclear (closed squares) and antiferromagnetic (open ovals) peak positions in the (H0L) and (0KL) scattering planes, in zero field.

We have determined that the spin direction is along **a** by analyzing the **Q** dependence of the magnetic Bragg peak
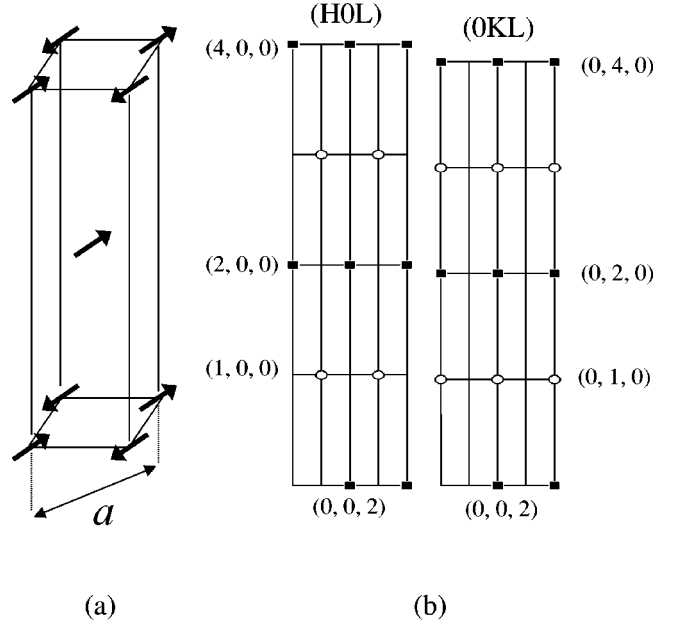

FIG. 2. (a) Antiferromagnetic spin arrangement below T_N. The spins lie along the orthorhombic **a** direction and all spins in the same *ac* plane point in the same direction. (b) Allowed nuclear (dark squares) and antiferromagnetic (ovals) reflections in the (H0L) and (0KL) zones. The orthorhombic distortion is exaggerated for clarity. Superlattice reflections which result from the fourfold increase in the unit cell along **a** are not shown.

intensity for various scattering geometries. For a collinear spin arrangement, the magnetic cross section is given by

$$\frac{d\sigma}{d\Omega} \propto (\gamma r_0)^2 (\tfrac{1}{2} g \mu_b)^2 (F(\mathbf{Q})\langle \mathbf{S} \rangle \sin(\alpha))^2 \left(\sum_d e^{i\mathbf{Q}\cdot\tau_d} \right)^2 .$$

(1)

In (1), $F(\mathbf{Q})$ is the magnetic form factor, which is the same for the four spins in the magnetic unit cell.[20] τ_d denotes the position of each spin and the sum in (1) is the structure factor, $S(\mathbf{Q})$. Each spin has expectation value $\langle \mathbf{S} \rangle$ and α is the angle between $\langle \mathbf{S} \rangle$ and the momentum transfer vector, $\mathbf{Q}$. Figure 3 shows the L dependence of the integrated intensity of the AF peaks along (1, 0, L). The integrated intensity at the Bragg position (1, 0, L = odd) grows with increasing L because of the increasing perpendicular component of $\mathbf{Q}$ with respect to $\langle \mathbf{S} \rangle$. From Fig. 3 it is clear that the staggered moment is along **a**, rather than along **b**, as proposed by Tarascon *et al.*[15]

The temperature dependence of the intensity of the (1, 0, 1) Bragg peak, which is proportional to the square of the Co^{3+} ordered moment, is shown in Fig. 4(a). The data are fit to an order parameter function with a Gaussian distribution of Néel temperatures. Although a good fit ($\chi^2 < 1$) is obtained, the substantial rounding near the transition temperature prevents an accurate determination of the order parameter exponent, β. Several fits to the data with $\chi^2 \lesssim 1$ are shown. The solid line is the result of a fit with β fixed at 0.25, the value observed in many 2D square-lattice Heisenberg systems,[21] and a fitted $T_N = 218(2)$. The dotted line is a
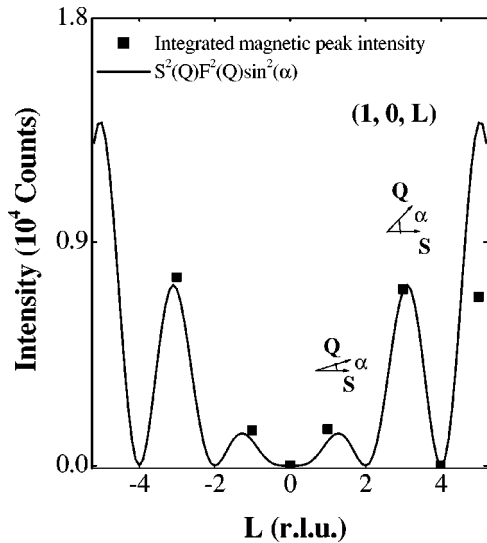
FIG. 3. Integrated intensities measured at the AF Bragg positions are proportional to the magnetic cross section, $F^2(\mathbf{Q})S^2(\mathbf{Q})\sin^2(\alpha)$ (solid line), where $S(\mathbf{Q})$ is the $\mathbf{Q}$-dependent structure factor. Shown here is a scan along L through $(1, 0, L)$. The intensity is maximized when $\mathbf{Q}$ and $\mathbf{S}$ are orthogonal, which explains the increase in intensity with L. The drop off in intensity for $L = 5$ is mostly due to an incomplete vertical integration of the signal caused by the fairly large mosaic in this crystal. This effect is most severe at large $|\mathbf{Q}|$.

fit with β fixed at 0.12, the value for the 2D Ising model, and a fitted $T_N = 208(1)$. Finally, the dashed line is a fit with T_N fixed at 235 K, the transition temperature determined from the susceptibility, and a fitted value of $\beta = 0.425(0.031)$. All fits have a Gaussian distribution of Néel temperatures with variance $\sigma \sim 30$ K. The origin of the rounding is most likely inhomogeneity of the oxygen content for this as-grown crystal, since annealed samples show narrower transitions ($\sigma \sim 10$ K) .

In Fig. 4(b), the peak intensity of a scan through the rod arising from two-dimensional AF spin fluctuations is plotted as a function of temperature. This measurement is made in the 2-axis mode without energy analysis, such that the detector integrates over all final neutron energies.[22] The transfer of weight out of the rod and into the Bragg peaks at ~ 250 K can be seen by comparing Figs. 4(a) and 4(b). The two-dimensional magnetic scattering near the 3D ordering temperature is similar to that found in the Heisenberg antiferromagnet La$_2$CuO$_4$.[21] In particular, the reduction of the quasielastic intensity at $(1, 0, 0.4)$ as the temperature is lowered below T_N is more gradual than the observed critical behavior of K$_2$NiF$_4$, a prototypical 2D Ising system.[23] However, the rounding at the transition resulting from inhomogeneity of the oxygen may obscure the true critical behavior.

The magnitude of the ordered Co^{3+} moment, $\langle M_{AF}\rangle$, is estimated by normalizing the AF peak to the nuclear $(0, 0, 2)$ reflection, which has a known cross section.[15] We estimate $\langle M_{AF}\rangle = 2.5 \pm 0.8$ μ_b/Co resulting in $\langle S_{AF}\rangle = 1.3 \pm 0.4$ μ_b/Co, assuming g = 2. The estimated moment is closest to the intermediate spin state, S = 1, of the Co^{3+} ion in an octahedral crystal field. Preliminary spin wave mea-
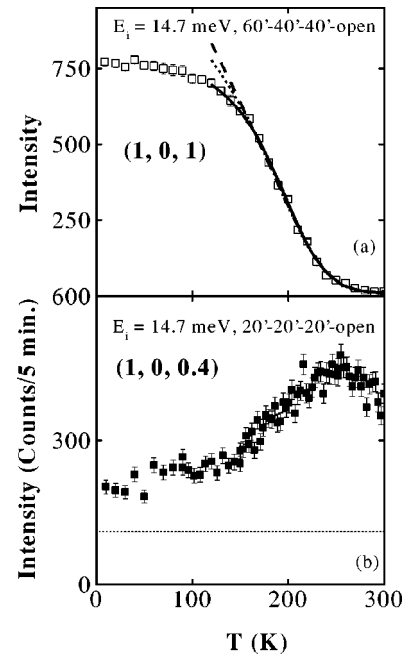

FIG. 4. (a) Integrated intensity at the $(1, 0, 1)$ AF reflection measured as a function of temperature. The three curves are fits of the data, for T$>$150 K, to an order parameter function with a Gaussian distribution of transition temperatures. The curves correspond to a fit with β fixed at 0.12 (dark line), β fixed at 0.25 (dotted line), and T_N fixed at 235 K (dashed line). (b) Peak intensity of a scan through the rod of 2D AF scattering as a function of temperature; the dashed line is the background, measured at $(1.077, 0, 0.4)$ at 30 K.

surements provide an estimate of ~ 13 meV for the in-plane AF exchange interaction (using $\langle S\rangle = 1.3$).

B. Ferromagnetism in Bi$_2$Sr$_2$CoO$_{6+\delta}$, $\delta \sim 0.25$

Bi$_2$Sr$_2$CoO$_{6+\delta}$ with $\delta = 0.25$ is expected to have equal amounts of Co^{2+} and Co^{3+}. The distinguishing feature of a sample with nominal composition Bi$_2$Sr$_2$CoO$_{6.25}$ is the absence of AF peaks found in Bi$_2$Sr$_2$CoO$_{6+\delta}$, $\delta > 0.4$; a scan along $(0, 1, L)$ shows no temperature dependence between 5 K and 300 K. This indicates that NN spins in the ab plane no longer have an AF coupling. The crystal with this composition instead shows predominantly ferromagnetic behavior in the ab plane.

Figure 5(a) shows a measurement of the temperature dependent susceptibility with the applied field H along **a**, **b**, and **c**. For the susceptibility along **a**, both zero-field cooled (ZFC) and field-cooled (FC) measurements are shown. The thermal hysteresis occurring below 30 K is only seen at low fields and may indicate spin-freezing; we will focus on the magnetization above 30 K where the thermal hysteresis is not observed. The susceptibility indicates a strong in-plane spin anisotropy, with the largest susceptibility along **a** and a much smaller susceptibility along **c**. Although there is a sharp decrease in the susceptibility at 47.5 K, this does not result from an AF ordering of neighboring spins in the ab plane, as discussed above.

A Curie fit of χ_a at high temperature (>300 K) yields a FM Curie temperature $T_c \sim 100$ K, and $\mu_{\text{eff}} \sim 4\mu_b$ per Co.
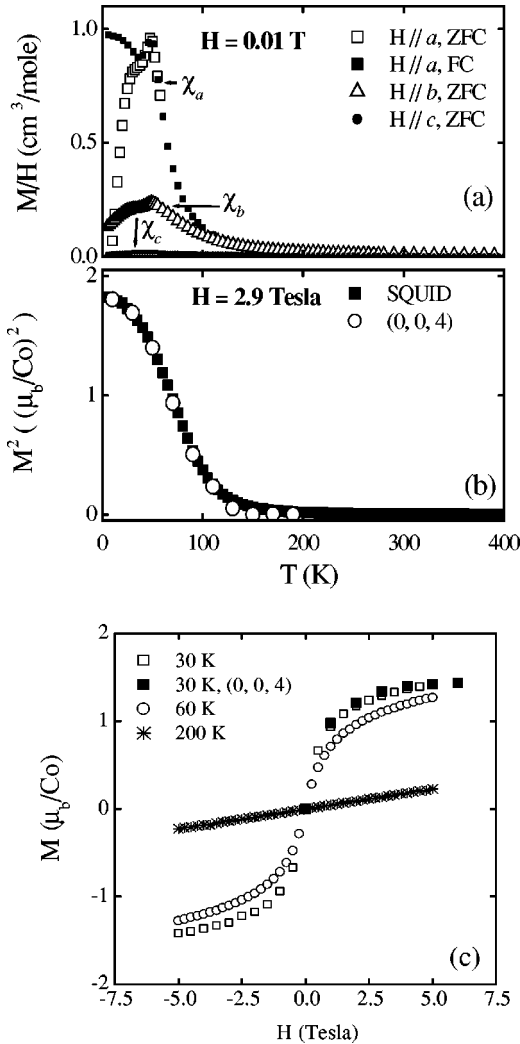
FIG. 5. (a) Temperature dependent susceptibility of a $\delta \approx 0.25$ crystal. Both field-cooled (FC) and zero-field cooled (ZFC) susceptibilities are shown for χ_a. (b) Temperature dependence of the square of the uniform moment measured in the SQUID (dark squares) and the magnetic contribution to the intensity at the (0, 0, 4) Bragg peak (open circles) in a 2.9 T field along **a**. (c) The field dependence of the uniform moment measured in the SQUID for H along **a** at 30, 60, and 200 K. Also shown is the field dependence of the square root of the intensity of the magnetic scattering at (0, 0, 4) (large squares), normalized to the SQUID data at 5 T.

For $T \gg T_c$ we can treat the paramagnetic susceptibility as arising from two sublattices, one with the spin of the Co^{2+} and the other with the spin of the Co^{3+}, which are ferromagnetically coupled. We find that the fitted value for μ_{eff} is greater than the value expected for either an equal mixture of Co^{3+} in the S = 1 state and Co^{2+} in the S = 3/2 state (μ_{eff}=3.39) or an equal mixture of Co^{3+} in the S = 2 state and Co^{2+} in the S = 1/2 state (μ_{eff}=3.67), but less than the value expected for Co^{3+} in the S = 2 state and Co^{2+} in the S = 3/2 state (μ_{eff}=4.42). We note that the μ_{eff} values expected for Co^{2+} in the S = 1/2 state and Co^{3+} in the S = 1 and 0 state are 2.35 and 1.22, respectively, which are much smaller than the fitted μ_{eff}.

In Fig. 5(b), the square of the uniform moment in a 2.9 T field is plotted as a function of temperature. (We plot the square of the moment for ease of comparison with the neutron results.) In this measurement, the field is applied along **a**, the direction which shows the largest susceptibility. The temperature dependence is suggestive of a ferromagnetic ordering with an onset near 100 K, consistent with the above Curie fit. Note, however, that the temperature dependence of the moment is strongly field dependent; in particular, the zero field measurement in Fig. 5(a), as well as the zero field neutron data (shown below), reveal no net moment.

To explore a possible ferromagnetic ordering of the spins with neutrons, we measure the magnetic contribution to the intensity at the allowed nuclear reflections [see Fig. 2(b)]. All of the measurements are performed in the (0KL) plane with the field along **a**. Since the magnetic intensity is weak compared to the nuclear intensity, we have chosen to look for ferromagnetism at relatively weak structural positions. The (0, 0, 4) nuclear position is ideal, as it is sufficiently weak that the magnetic intensity is at least 10% of the nuclear intensity and $|\mathbf{Q}|$ is small so that the form factor remains large.

The temperature dependent ferromagnetic contribution to the intensity of the (0, 0, 4) Bragg peak induced by a 2.9 T field is shown in Fig. 5(b). The field is necessary because, as noted above, the uniform moment vanishes at H = 0. We determine the ferromagnetic contribution to the intensity at (0, 0, 4) as the difference between the total intensity and the intensity at 190 K, at which temperature the intensity at this position is completely due to nuclear scattering. This is confirmed by the absence of field dependence at 190 K. The neutron data are normalized to the SQUID data at 30 K to show that both quantities have the same temperature dependence. We note that the temperature dependence measurement in Fig. 5(b) does not constitute a true order parameter measurement of ferromagnetic ordering since the measurement is not made at zero field. The absence of a spontaneous ferromagnetic moment in zero field indicates that the vector sum of the four spins in the magnetic unit cell is zero at zero field. The moment measured in Fig. 5(b) is therefore more appropriately called a field-induced ferromagnetic moment.

Figure 5(c) shows a SQUID measurement of the moment vs field at 30, 60, and 200 K, again with the field applied along **a**. Above ~ 150 K, the moment is linear in field up to 5 T. Also plotted in Fig. 5(c) is the field dependence of the uniform moment measured by neutrons at 30 K. Again, the neutron data have been normalized to the magnetization at 5 T to emphasize that the field dependence is the same for both measurements. The absolute moment determined from neutrons is 2.1±0.7 μ_b per Co at 5 T, which is within error of the moment of 1.5±0.1 μ_b/Co measured by the SQUID.

The field dependence of the moment at low T shown in Fig. 5(c) is unusual; the size of the moment increases rapidly up to 2 T and then shows a much slower increase at fields up to 7 T without saturating. The field dependence of the uniform moment is similar to that expected for a soft ferromagnet, i.e., a ferromagnet with a small coercive field; however, a ferromagnet has a finite microscopic moment at H = 0 which can be seen by neutrons even if the uniform moment

vanishes because of domain effects. That is, the intensity of the neutron peaks and the bulk magnetization would not coincide for a soft ferromagnet as they do in Fig. 5(c). Therefore, we conclude that the field induces a continuous polarization of the spins from a zero-moment ground state.

The size of the moment at 5 T is 1.5 ± 0.1 μ_b/Co, which in the simplest picture is the expected moment for either an equal mixture of S = 0 and S = 3/2 spins or S = 1 and S = 1/2 spins. As in the Curie fit, we cannot determine uniquely the separate spin on the Co^{2+} and Co^{3+} sites from the total (bulk) saturated moment.

Since the ferromagnetic Curie temperature and the nonlinear field dependence suggest that the dominant interaction is ferromagnetic, we propose that the absence of a uniform moment at zero field results from a small AF coupling along **c** between ferromagnetic layers. This would explain the large ferromagnetic susceptibility at high temperatures seen in χ_a and the suppression of the moment below 47.5 K. We note that this proposed spin arrangement would result in magnetic Bragg peaks at the (0, 0, L = odd) positions at zero field. Preliminary measurements in which (0, 0, L = odd) peaks are observed to disappear in a magnetic field confirm this picture.[24] In the following section, evidence is presented for other samples that an antiparallel stacking of the layers is, indeed, the zero-field ground state for the $\delta \sim 0.25$, FM phase.

C. Doping dependence, $0.25 < \delta < 0.5$

The compositions $Bi_2Sr_2CoO_{6.5}$ and $Bi_2Sr_2CoO_{6.25}$ appear to be two end points in the phase diagram of $Bi_2Sr_2CoO_{6+\delta}$. We have shown that the $\delta \gtrsim 0.4$ crystal with mostly Co^{3+} spins undergoes a transition to an antiferromagnetic alignment of the spins in the ab plane with $T_N > 200$ K. On the other hand, the $\delta \simeq 0.25$ crystal has nearly equal numbers of Co^{3+} and Co^{2+} ions and the in-plane interaction is ferromagnetic with $T_c \sim 100$ K. To study the evolution of the magnetism between these two end-point compositions, we have characterized samples which have been annealed to give a range of Néel temperatures from 295 to 0 K.

Figure 6 shows the magnetic susceptibility with the field applied along **a** for samples which have T_N ranging from 295 K to 0 K. The enormous growth of the ferromagnetic-like peak with decreasing T_N suggests that the ferromagnetic interaction is favored by removal of oxygen from $Bi_2Sr_2CoO_{6+\delta}$ and competes with the antiferromagnetic order found in samples with $\delta > 0.4$. As discussed below, the peak in the susceptibility occurs at the same temperature as T_N for $T_N \gtrsim 125$ K. On the other hand, the two curves with the peak in the susceptibility occurring near 45 K correspond to two different samples, one with $T_N = 81.5$ K (dark squares, $T_{peak} = 40$ K) and one with no AF ordering (open circles, $T_{peak} = 47.5$ K). So as not to cause confusion, we will distinguish between T_{peak}, the temperature coinciding with the peak in the susceptibility, and T_N, which is the onset temperature for the sublattice magnetization measured by neutrons. For all of the samples shown in Fig. 6, the susceptibility at temperatures above the peak can be fit to a
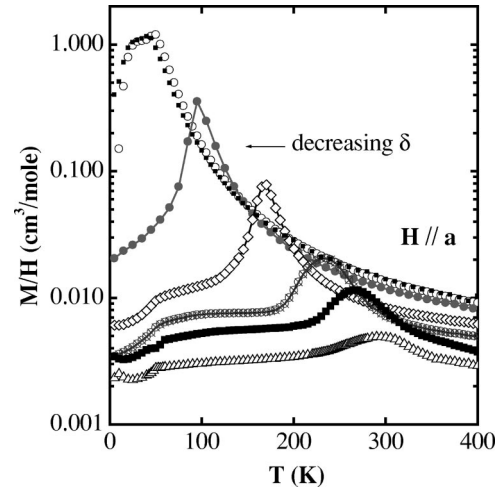

FIG. 6. Semi-logarithmic plot of the temperature dependent susceptibility for H parallel to **a** (the AF spin direction) for samples annealed in vacuum or oxygen to yield different oxygen content, δ. Starting from the right, the peaks in the susceptibility occur at temperatures, T_{peak}, equal to 295, 270, 235, 170, 95, 47.5, and 40 K. The samples with $T_{peak} = 270$ and 235 K were measured as-grown. The samples with $T_{peak} = 170$ and 95 K were annealed in <10 mTorr vacuum at 600 and 750 °C, respectively. The two samples with lowest T_{peak} were annealed in an evacuated quartz tube with Cu powder as a reducing agent. The sample with $T_{peak} = 295$ K was first reduced using the quartz tube method and then annealed, at 800 °C, in a flow of pure oxygen.

Curie–Weiss form with a ferromagnetic Curie temperature, T_c. T_c coincides with T_{peak} for $T_{peak} > 100$ K, while for T_{peak} below 100 K, T_c remains at 100 K even though T_{peak} continues to decrease.

We have already discussed the AF spin ordering of a sample with $\delta > 0.4$ and $T_N > 200$ K. From Fig. 6, it is clear that the ferromagnetic peak, though much reduced compared to the $\delta \sim 0.25$ phase, is present for these high T_N samples as well. Therefore, we first focus on understanding the presence of ferromagnetism in samples which have nominally high δ ($\delta > 0.4$) and well defined AF transitions, before discussing the full doping dependence of the magnetism for $0.25 < \delta < 0.4$.

The temperature dependent magnetic susceptibility of the same crystal used to determine the AF spin structure (Figs. 3 and 4) is shown in Fig. 7. The inset shows the spin orientation in a single magnetic layer, determined from the neutron measurements discussed previously. Both zero-field cooled and field-cooled measurements of χ_a, χ_b, and χ_c in a 0.1 T field are shown, with the largest difference between zero-field cooling and field cooling occurring when the field is along **a**. The peak in the susceptibility along **a** at $T_{peak} = 235$ K is identified as the transition to 3D AF order because of the sharp drop in the susceptibility below this temperature. The Néel temperature determined in this way is close to that measured by neutrons, and we have already shown that taking T_N to be 235 K gives a satisfactory fit to the neutron data [see Fig. 4(a)].

The susceptibility is also highly anisotropic, and while the c-axis susceptibility is small and nearly temperature indepen-
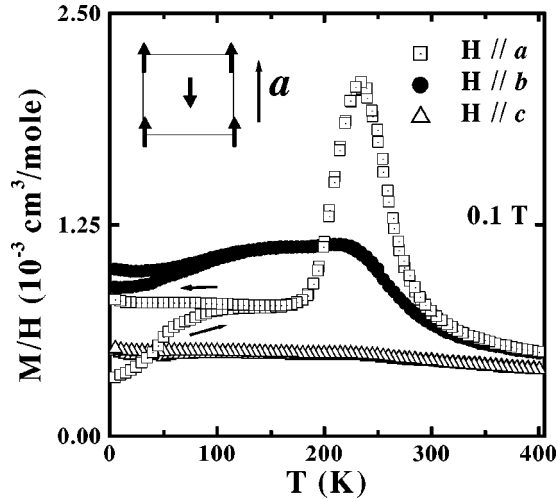
FIG. 7. Temperature dependent magnetic susceptibility of a sample with $T_N \simeq T_{peak} = 235$ K for H parallel to **a**, **b** and **c**. The susceptibility along **a**, and to a lesser extent, **b**, shows ferromagnetic behavior above 235 K, while the c-axis susceptibility is nearly temperature independent. The inset shows the spin arrangement in the AF phase in a single layer.

FIG. 8. (a) Field dependence of a sample with $T_{peak} = 215$ K at 180 and 50 K with the field applied along **a**. The maximum in dM/dH for the 180 K scan determines the critical field H_c, which is 1.6 T for this sample. (b) Comparison between the moment at 5 T measured after cooling in zero field (ZFC) and after cooling in a field (FC).

dent, the susceptibility shows ferromagnetic behavior when the field is along **a**, and, to a lesser extent, when the field is along **b**. At temperatures above the peak in χ_a (T $\geqslant 300$ K), the susceptibility is well described by a Curie–Weiss form with a ferromagnetic $T_c \simeq T_{peak} = 235$ K and $\mu_{eff} = 1.4\mu_b$, assuming all Co ions contribute.

The result of the Curie fit is surprising both because of the difference in sign between the fitted Curie temperature and that expected for AF exchange and the small magnitude of the Curie constant (for S = 1 and g = 2, one expects $\mu_{eff} = 2.8$). In addition, the existence of a FM peak along the easy axis of the AF is difficult to explain. A peak in the susceptibility of an AF is usually an indication of a competing FM interaction, which gives rise to a canted moment. For example, such weak ferromagnetism is observed in La_2CuO_4 because of the Dzyaloshinsky–Moriya interaction between neighboring spins, which causes the spin to cant out of the plane.[25] However, the canting resulting from such a mechanism is perpendicular to the AF spin direction, while in $Bi_2Sr_2CoO_{6+\delta}$, the enhanced susceptibility is strongest *along* the AF spin direction. Furthermore, for ferromagnetism resulting from canting, the size of the canted moment should be intrinsic to the AF order. It is clear from Fig. 6 that the size of the FM peak grows as T_N is suppressed, whereas one would expect the staggered moment, and therefore the canted moment, to decrease as T_N decreases.

The field dependence of the moment, M(H), for $T < T_N$ suggests ferromagnetism which is hidden at zero field. M(H) with H along **a** and T = 180 K is shown in Figure 8(a) for a sample with a similar susceptibility to that shown in Fig. 7, with $T_N \simeq T_{peak} = 215$ K. At low fields, the moment is linear in field. Near 1.6 T, there is a large jump in the moment which corresponds to $\sim 0.25\mu_b$ per Co for the field sweep at 180 K. We define the maximum in dM/dH as the "critical field," H_c, for the jump in the moment.
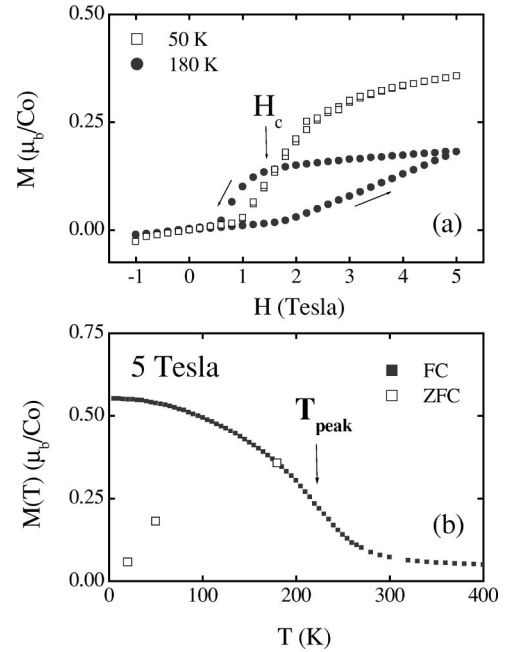
The comparison between M(H) at 180 K and 50 K in Fig. 8(a) shows that the hysteresis grows substantially with decreasing temperature. (Below 10 K there is no sign of a deviation from a constant susceptibility up to 5 T, suggesting that the hysteresis is larger than the range of the field used in the measurement.) The growing hysteresis with decreasing temperature is consistent with the observed difference between field cooled and zero-field cooled measurements of the susceptibility. We note that when the field is applied along **b** or **c** the moment is linear with field up to 5 T at all temperatures. This suggests that the jump in the moment is closely related to the FM behavior since the susceptibility data show the largest peak when the field is along **a**.

Figure 8(b) shows the moment as a function of temperature while cooling in a 5 T field. The moment vs temperature in the field cooled measurement resembles that of a ferromagnet. As discussed previously, this measurement is made at high field and does not indicate the onset of a spontaneous moment; the absence of a FM moment for H = 0 has been confirmed with neutrons. Rather, the measurement in Fig. 8(b) shows the temperature dependence of a field induced ferromagnetic moment. The inflection point of M(T) in the field-cooled measurement is at the same temperature as T_N measured in zero field, suggesting that the field induced FM behavior only occurs in the ordered phase of the AF. For comparison, the moment obtained at 5 T after cooling in zero-field is also shown. The data show a substantial difference between the field cooled and zero-field cooled moment for $T < 200$ K, which may indicate that the low-field to high-field transition is first order in nature.
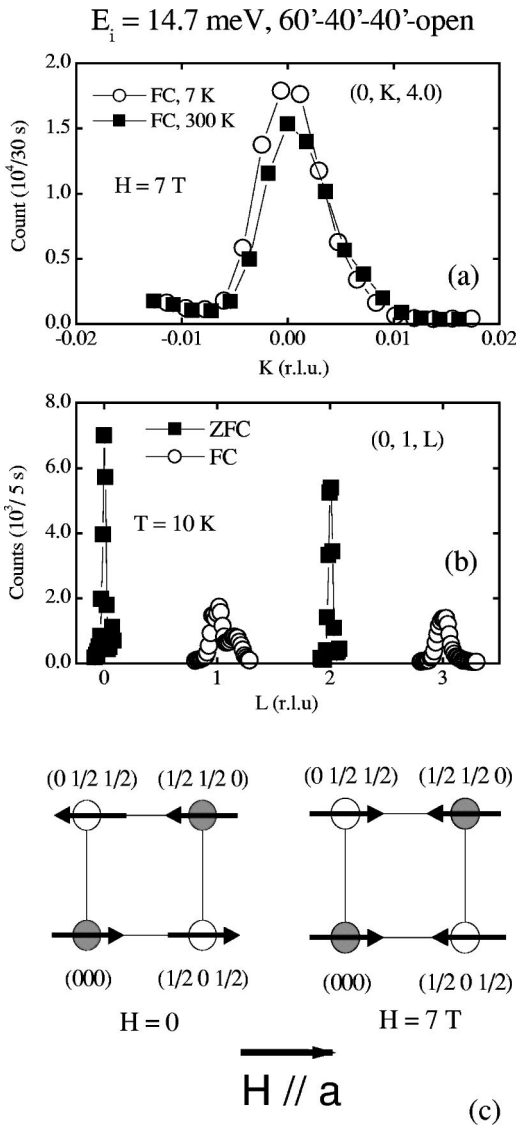
FIG. 9. Applying a 7 T magnetic field along **a** results in (a) increased scattering at the (0, 0, 4) nuclear peak, shown here at 7 K and 300 K and (b) a shift in the AF peaks from the zero-field positions (0, 1, L = even) to the high field positions (0, 1, L = odd). The double peaks at low L in the scan in (b) result from a second nearby crystallite. The shift in the positions of the AF peaks likely result from a change in the inter-plane stacking of the spins as indicated in the sketch in (c). The shaded circles and open circles are in adjacent layers separated by $c/2$. The arrow indicates the direction of the field, which is parallel to **a**.

Field-dependent neutron scattering measurements reveal both FM and AF Bragg peaks above H_c for the sample studied in Fig. 8. We first discuss the field induced FM peaks. The scattering geometry is such that the field is applied along **a**, as in the SQUID measurement, and the scattering plane is (0KL). After cooling in 7 T, we observe enhanced scattering at the (0, 0, 4) nuclear position, resulting from a FM alignment of the spins, just as for the $\delta \sim 0.25$ sample. In Fig. 9(a), a transverse scan (along K) through the (0, 0, 4) nuclear position is shown for H = 7 T at 300 K and after field cooling in 7 T to 7 K. There is a clear enhancement of the

scattering in the 7 K scan compared to the 300 K scan. In a similar sample, we have confirmed that the field induced intensity at the (0, 0, 4) peak results from FM scattering by performing polarized neutron scattering without spin analysis.

The magnetic field also affects the AF structure. Figure 9(b) shows a scan along L through (0, 1, L) at 10 K after cooling in zero field and after cooling in 7 T. When the sample is cooled in zero field, there are AF Bragg peaks at the L = even positions just as in Fig. 2(b). After cooling in a 7 T field, these peaks disappear and new AF peaks appear at the L = odd positions, indicating a high field AF phase with a different spin arrangement than the H = 0 phase. The positions of the high field AF peaks are consistent with a 180° rotation of all of the spins in alternate layers of the low-field AF. This change in the stacking arrangement is indicated in Fig. 9(c), which shows a projection diagram of all four spins in the magnetic unit cell.

The high field AF peaks have a significantly smaller peak intensity and are nearly twice as broad as the AF peaks in zero field, i.e., the high field AF peaks are no longer resolution limited. Comparing the integrated intensity of the (0, 1, 0) peak after zero-field cooling and the (0, 1, 1) peak after cooling in 7 T, we find that the scattering is nearly conserved when the field is applied. The broadening of the AF peak only occurs in the L direction, which implies that the antiferromagnetic order at high field has a smaller magnetic correlation length along **c** than that at zero field. To analyze the peak widths, we define the correlation length as the inverse of the half-width at half-maximum (HWHM) of a Gaussian line shape in Q, which is convoluted with the spectrometer resolution function to obtain the experimentally observed peak in Q space. The correlation length determined for the different magnetic Bragg peaks can then be compared. We estimate that the magnetic correlation length, ξ_c, for the high-field AF is ~ 80 Å, compared to ≥ 400 Å for the zero-field cooled, resolution limited AF peaks

In Fig. 10(a), the field dependence at 180 K of the (0, 1, 0) and (0, 1, 1) AF peaks and the square of the uniform moment, as measured in the SQUID, are shown. Clearly, the AF structure and the magnitude of the uniform moment both show strong variations at approximately the same field. However, the magnetic peaks observed at the positions (0, 1, 1) and (0, 0, 4) cannot be caused by scattering from different components of the same ordered moment (i.e., a field induced ferrimagnet or spin-flop of the antiferromagnet) because the peaks have different correlation lengths along **c**. At high magnetic field, the peaks at the AF positions are not resolution limited and have $\xi_c \sim 80$ Å while the FM peaks are resolution limited and have $\xi_c \geq 120$ Å. This is an important point because it indicates that there are distinct AF and FM regions in this sample.

To further confirm that the observed peaks at the FM and high field AF reflections do not result from a canted AF, we have performed polarized neutron measurements on a similar sample. We have used a full polarization analysis set-up to measure, independently, the neutron spin flip (SF) and non-spin flip (NSF) cross sections for scattering from the ordered spins in the sample. The neutrons are polarized in the same
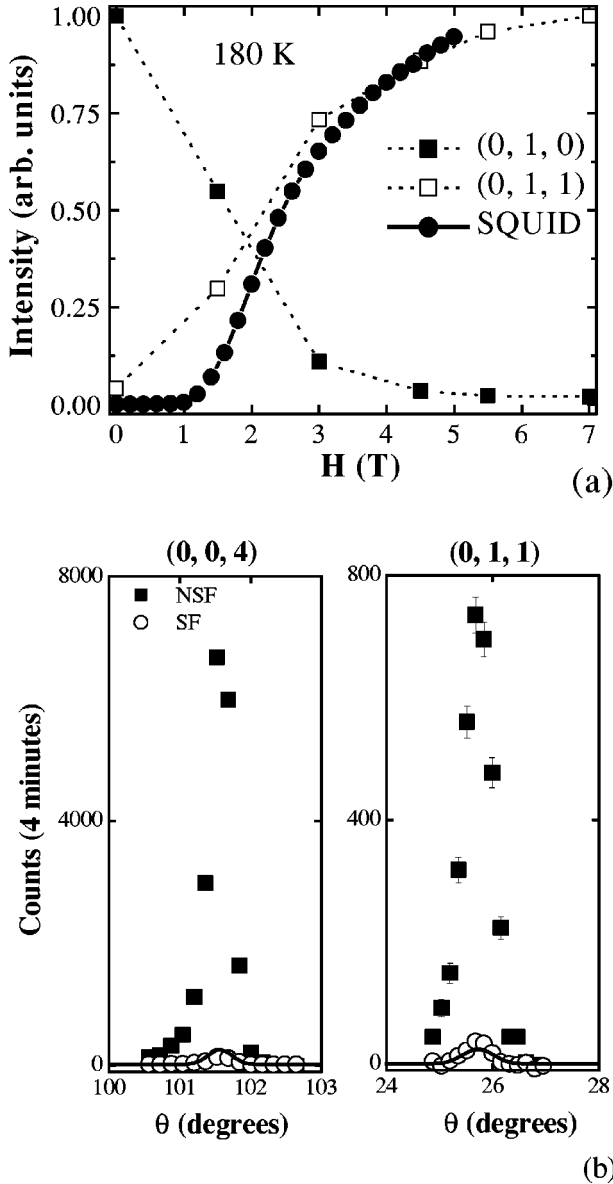
FIG. 10. (a) Field dependence of the intensity of the (0, 1, 0) and (0, 1, 1) AF peaks at 180 K. The square of the moment measured in the SQUID, from Fig. 8(a), is also shown. The increase in intensity of the (0, 1, 1) peak and the jump in the uniform moment occur at approximately the same magnetic field. (b) Measurement of spin-flip (SF) and nonspin flip (NSF) intensities of the (0, 0, 4) and (0, 1, 1) peaks in a full polarization set-up (see text). The dark line indicates the intensity of SF scattering expected from imperfect polarization. The experimentally determined polarization is 0.94.

direction as the applied field, which is along the *a*-axis of the sample. The beam's polarization may be determined by measuring the ratio of NSF to SF intensities at several structural reflections above T_c. We find that the polarization along **a** is 0.94 ± 0.01. [The polarization, P, is defined as $(F-1)/(F+1)$, where F is the ratio of neutrons with spin up to neutrons with spin down.] The SF and NSF cross sections of the FM (0, 0, 4) and AF (0, 1, 1) reflections are measured after cooling to 5 K in a 7 T field parallel to **a** and then reducing the field to 1 T (due to hysteresis, it is possible to reduce the field to 1 T without changing the high-field state).

In Fig. 10(b), scans through the (0, 0, 4) and (0, 1, 1) peaks are shown for both the NSF and SF configurations. Also indicated is the background expected from imperfect polarization. The absence of SF processes above the background at the (0, 0, 4) reflection indicates that the FM moment is collinear with the *a*-axis, as expected. At the AF (0, 1, 1) reflection, the amplitude of the peak in the SF configuration corresponds to 4.75% of the amplitude of the NSF peak, which is slightly higher than what is expected from imperfect polarization (3.3%).

We now explain why these results are inconsistent with a canting model. In a canted AF, the FM moment arising from a canting of AF spins is necessarily perpendicular to the direction of the staggered moment. Therefore, if the neutrons are polarized along the FM component of a canted AF, the neutron spin and staggered moment will be perpendicular to one another. Since a neutron's spin flips when scattered from a perpendicular moment, this situation will lead to 100% spin flip scattering at the AF reflections. In this situation, the ratio of SF to NSF scattering at the AF reflection will be given by $(1+P)/(1-P)\sin^2(\alpha)$, where α is the angle between the direction of the staggered moment and the momentum transfer vector, Q. We estimate that the SF scattering arising from an AF with a canted moment should be *at least* 1.4 times as great as the NSF scattering, i.e., the SF peak amplitude should be *greater* than the NSF peak amplitude.[26] The SF scattering seen at the (0, 1, 1) reflection in Fig. 10(b) is clearly much *less* than the NSF scattering. Therefore, the simultaneous FM and AF reflections seen at high field cannot result from a canted AF.

Although simultaneous FM and AF reflections could result from a collinear ferrimagnetic ordering, the ratio of the FM to AF peak intensity should not depend on the magnetic ordering temperature. As shown below, the suppression of the Néel transition temperature results in an increase in the FM moment relative to the AF (staggered) moment.

For the above reasons, we conclude that the FM and AF peaks result from distinct magnetic domains in the sample. To quantify the intensity of the FM and AF peaks in absolute units, we use the following normalization: The FM intensity at (0, 0, 4) is attributed to a uniform moment per Co ion, i.e., each Co site has a spin, $\langle S_{FM} \rangle$, which lies along **a**. The additional scattering at the position (0, 0, 4) is therefore proportional to $\langle S_{FM} \rangle^2$. Similarly, the intensity at the AF peak is attributed to a spin $\langle S_{AF} \rangle$ on each Co of each sublattice in an antiferromagnet domain. Since we believe that the origin of the FM and AF ordered moments arise from different domains, we should ideally normalize the magnetic intensity at the AF and FM peak positions to the number of spins in the AF or FM domain, respectively. Since we do not know *a priori* the volume of either domain, we normalize the intensity to the total number of Co ions in the crystal. However, our interpretation is that the two quantities, $\langle M_{AF} \rangle$ and $\langle M_{FM} \rangle$, describe distinct magnetic phases.

The magnetic cross section also depends on the direction of the magnetic spin with respect to the momentum transfer vector **Q** [Eq. (1)]. We have shown that the spin lies along **a** in both the AF and FM domains at all fields. Therefore all peaks measured in the (0KL) scattering plane have **Q** $\perp$ to
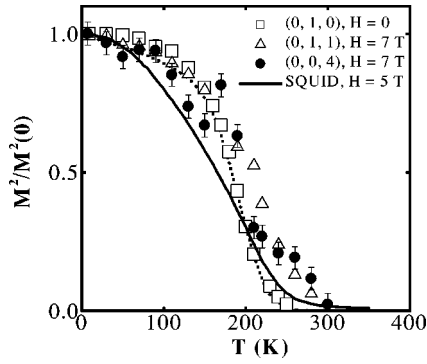
FIG. 11. Temperature dependencies of the (0, 1, 0) integrated intensity in zero field and the (0, 1, 1) and (0, 0, 4) integrated intensities in 7 T. The field is applied along **a**. The line through the temperature dependence of the (0, 1, 0) peak intensity is a guide to the eye. The uniform moment squared (dark line), measured in the SQUID at 5 T, is also shown.

$\langle S \rangle$ and $\sin^2 \alpha = 1$. We thus estimate that the FM moment for the sample studied in Figs. 8–10 is between 0.4 and $0.8 \mu_b$ per Co ion. The range of values represents the uncertainty in determining the absolute intensity of the different nuclear peaks for the normalization.

Figure 11 shows the temperature dependencies of the integrated intensity of the (0, 1, 0) peak in zero field, the (0, 1, 1) peak and the (0, 0, 4) peak in 7 T, and a SQUID measurement of the square of the uniform moment in a 5 T field for the above sample. The integrated intensities of the (0, 1, 0) and (0, 1, 1) peaks are proportional to the square of the ordered moment in the AF phase at zero and high field, respectively, while the integrated intensity of the (0, 0, 4) peak is proportional to the square of the ordered moment in the FM phase. All of the data are plotted in the form $M^2(T)/M^2(0)$. Remarkably, the ordering temperatures for the low and high field AF phases, as well as the FM phase, appear to be the same. At first sight, this appears to be at odds with our arguments for phase separation. However, we believe that the coincidence of the ordering temperatures can be explained by considering the interaction between the two magnetic domains, such that the ordering of one phase drives the ordering of the other. As we discuss below, the data suggest that the ordering of spins in the AF phase induces order in the FM phase.

We now discuss the observed growth in the ferromagnetic behavior as δ is reduced from $\delta > 0.4$ to $\delta \sim 0.25$. We have already shown that removal of oxygen not only suppresses T_N but enhances the ferromagnetic peak in χ_a by nearly two orders of magnitude between the sample with $T_{peak} = 295$ K and the sample with $T_{peak} = 47.5$ K (see Fig. 6). By comparing the neutron data to susceptibility measurements, we find that for samples with $T_{peak} \geqslant 125$ K, $T_{peak} \simeq T_N$, while for $T_N < 125$ K, T_{peak} and T_N differ. In addition, we find that T_c from the Curie fit of the paramagnetic susceptibility is $\simeq T_{peak}$ for $T_{peak} > 100$ K, while for samples with $T_{peak} < 100$ K, T_c remains fixed at $\simeq 100$ K even though T_{peak} decreases to 40 K. This suggests that the AF order determines the ordering of the FM phase when T_N is greater than 100 K, but when T_N is below 100 K, the FM and AF
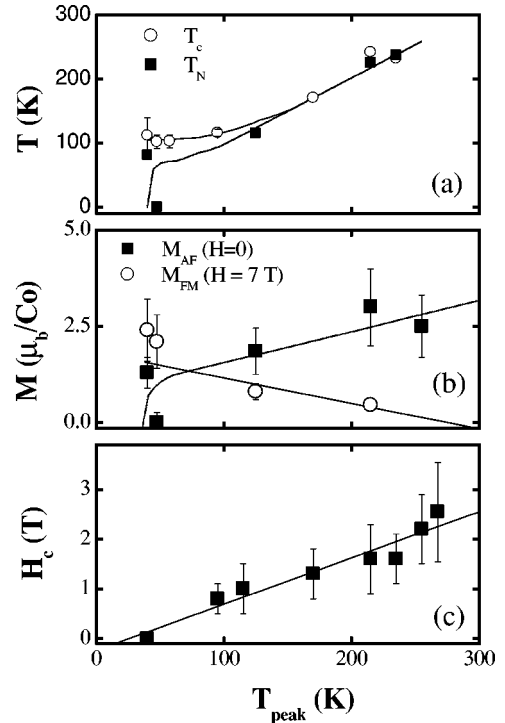

FIG. 12. (a) T_N, determined by neutrons, and T_c, determined from the Curie susceptibility, vs T_{peak}, the peak in the susceptibility. The lines are guides to the eye. Below $T_{peak} \sim 100$ K, T_c is constant while T_N drops abruptly to zero. (b) Calculated AF moment, $\langle M_{AF} \rangle$, and FM moment, $\langle M_{FM} \rangle$, as a function of T_{peak}. The point at $T_{peak} = 47.5$ K corresponds to the sample with no in-plane AF order, discussed in Sec. III B. The lines are guides to the eye. (c) The decrease in the critical field, H_c, with decreasing T_{peak}. The error bars correspond to the larger of the width of the transition (i.e., the HWHM of dM/dH) or the hysteresis.

orderering temperatures decouple with T_c determined by the intrinsic properties of the FM phase. These results are summarized in Fig. 12(a), where T_c and T_N are plotted as a function of T_{peak}. We use T_{peak} to differentiate samples with different oxygen content, since this is more easily measured than δ. We note that while the AF order is likely very sensitive near the composition $\delta \sim 0.25$, T_{peak} shows little variation. This may explain why we observe a slightly lower T_{peak} for the sample which has $T_N \sim 80$ K compared to the sample which has no observable long-range AF order. Since the substantial rounding near the onset temperature for AF ordering prevents a reliable fit of the data from sample to sample, we define T_N in Fig. 12(a) as the temperature at which the intensity of the AF Bragg peak is 10% of the maximum intensity. T_c is the FM Curie temperature determined from the Curie fits of the paramagnetic susceptibility. There are fewer points for T_N than T_c because we can only measure T_N with neutrons, while T_c is easily determined from the susceptibility.

In Fig. 12(b), the ordered AF moment at H = 0, $\langle M_{AF} \rangle = g \langle S_{AF} \rangle$, and the field induced uniform moment $\langle M_{FM} \rangle = g \langle S_{FM} \rangle$, determined from neutrons, are plotted as a function of T_{peak}. The data in Fig. 12(b) show that as oxygen is removed and T_N is suppressed the FM moment increases and the AF staggered moment decreases.

TABLE I. Calculated $\langle M_{AF} \rangle$ measured at zero-field and $\langle M_{FM} \rangle$ measured at 7 T. For comparison, the field induced FM moment measured in the SQUID at 5 K after cooling in 5 T is also shown. $\langle M_{AF} \rangle$, $\langle M_{FM} \rangle$, and the SQUID FM moment are all in units of μ_b/Co. Multiple entries for the same sample correspond to normalization to different nuclear peaks.

T_N (K)	M_{AF}	M_{FM}	M_{FM} SQUID
237	2.5±0.8 [a]	⋯	⋯
225	2.4±0.8 [b]	0.45±.15 [b]	0.38
	3.7±1.2 [c]	0.8±.3 [c]	
115	1.9±0.7 [b]	0.8±0.2 [b]	⋯
	1.8±0.7 [c]	0.6±0.2 [c]	
81.5	1.3±0.4 [b]	2.1±0.7 [b]	1.7
	1.3±0.4 [c]	1.9±0.6 [c]	
No in-plane	⋯	2.4±0.8 [b]	1.75
AF order		1.9±0.6 [c]	

[a]Normalized to the (002) nuclear Bragg peak.
[b]Normalized to the (004) nuclear Bragg peak.
[c]Normalized to the (020) nuclear Bragg peak.

Table I shows the calculated magnetic moment from magnetic neutron scattering measurements compared with the moment measured in the SQUID magnetometer. There is some variation in the magnetic moment calculated from the neutron peaks depending on which nuclear peak is used for normalization. This probably results from extinction effects. For most samples, the table shows two entries, one for normalization with the (0, 0, 4) nuclear peak, which is a weak nuclear reflection, and the second line for normalization with the (0, 2, 0) nuclear peak, which is a strong nuclear reflection. The errors correspond to ±30%.

Figure 12(c) is a plot of the critical field, H_c, as a function of T_{peak}. Since the critical field can only be measured by first cooling the sample in zero field to below T_N and then measuring the field dependence, there is some error in determining H_c at low temperatures because of the hysteresis. To avoid hysteresis, the critical field is measured for temperatures within 25% of T_N. The critical field appears to vanish for samples with T_{peak} between 95 K and 45 K, which is the same temperature range over which T_N and T_{peak} appear to decouple. This suggests that the critical field depends on the fraction of the sample that is in the AF phase.

Figure 13 shows the temperature dependencies of the integrated intensity of the (0, 1, 0) Bragg peak at H = 0 and the (0, 1, 0) and (0, 0, 4) peaks at 7 T for samples with $T_{peak}(T_N) = 215(225)$, 125 (115), 40 (81.5), and 47.5 (0) K. The solid line in Fig. 13 is the square of the uniform moment measured in the SQUID in a FC measurement (5 T). The dotted line is used to emphasize the (0, 1, 0) data, which reflect the zero-field AF order parameter. In (a) and (c) the SQUID data show a more rapid fall off with temperature than indicated by the (0, 0, 4) Bragg peak. This may reflect the lower field available for the SQUID measurement. There are no SQUID data available for the sample in (b). In (c) the temperature dependence of the (0, 1, 1) peak at high field is not shown because we did not take these data and in (d) there is no peak at (0, 1, 1), consistent with the disappearance of
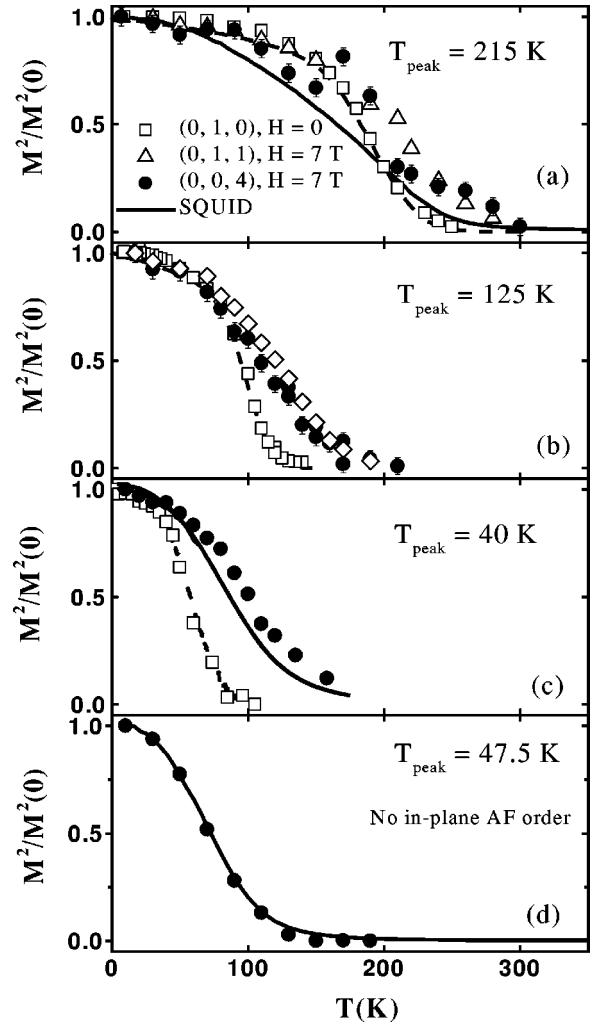

FIG. 13. Temperature dependence of the (0, 1, 0), (0, 1, 1), and (0, 0, 4) integrated intensities measured in samples with (a) T_{peak} $(T_N) = 215$ K (225 K), (b) 125 K (115 K), and (c) 40 K (81.5 K), and (d) for a sample in which no AF order of the Co^{3+} spins is measured. The SQUID measurement, at 5 T, is shown as a solid curve for each case, except for (d) where a 2.9 T field is applied for both the SQUID and neutron measurements. All measurements in a magnetic field are measured after field-cooling. The data are normalized at base temperature.

the Co^{3+} AF order. The data clearly show that when the Néel temperature is below about 125 K, the FM order is independent of the Néel ordering: Comparing (c) and (d), the onset temperature for the FM moment occurs at approximately the same temperature, even though the AF ordering has disappeared in (d).

We have not, up to this point, considered the zero field behavior of the FM domains in a sample exhibiting phase separation. As discussed above, the FM scattering measured at the nuclear positions disappeared below the critical field. It was therefore necessary to search for FM scattering at other Q positions. The measurements of the $\delta = 0.25$ FM sample suggested that the reduction of the moment to zero in zero field resulted from an AF interaction between FM layers. This type of AF stacking would be characterized by magnetic Bragg peaks at the positions (H = even, K = even,
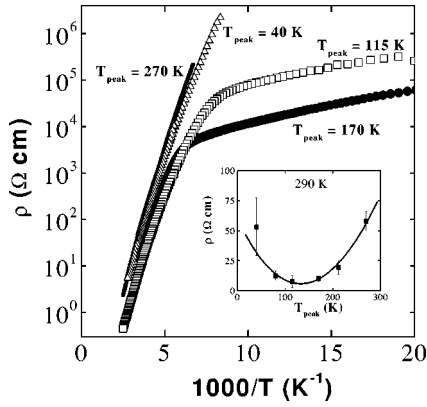
FIG. 14. Temperature dependent resistivity for samples with different T_{peak}. Samples with different T_{peak} show the same activated behavior, with activation energy ~ 250 meV. The inset shows the resistivity measured at 290 K as a function of T_{peak}. The error bars result from uncertainty in the geometric path of the current in the 4-probe measurement.

L = odd). We have therefore made preliminary measurements to look for magnetic peaks at these positions in a sample exhibiting phase separation. In the $T_N \simeq T_{peak}$ = 215 K sample (see Fig. 8), we found magnetic peaks at the (0, 0, L = odd) reflections, in zero field, which disappeared at the Néel transition. Unfortunately, this scattering setup did not include a magnetic field, and it was not possible to check that the peaks shifted to (0, 0, L = even) at the critical field. However, the zero field peaks at (0, 0, L = odd) showed the same intensity as the high field FM peaks at (0, 0, L = even) measured in a different setup. Similar behavior has also been observed in another sample with different T_N.

Although more work remains to be done to unambiguously identify the zero-field magnetic structure of the FM phase, the measurements described above provide fairly strong evidence for an antiparallel stacking of adjacent FM layers at zero-field. We note that the three dimensional ordering of the FM domains at the same temperature as the AF domains implies an interaction between the two domains. We will discuss this in more detail below.

Given the dramatic changes in the magnetism, it is surprising that the resistivity is relatively insensitive to doping. Figure 14 shows the temperature dependent resistivity for samples with a range of AF ordering temperatures. On this Arrhenius plot, all of the resistivity curves have the same slope above 200 K indicating a constant activation energy, $E_a \sim 0.25$ eV. There is no feature in $\rho(T)$ at T_{peak} for any of the samples, suggesting that the magnetic order has no significant effect on the transport. The inset shows the magnitude of the resistivity measured at 290 K, for which there is a distinct minimum for samples with T_{peak} near 115 K. The resistivity curves for T_{peak} = 175 and 115 K show a crossover to more weakly activated behavior with decreasing temperature, which may be related to the minimum in resistivity. Although crystals with low T_N are expected to have large FM domains, there is no evidence for a transition to metallic behavior as one finds in the manganites. We note that the related compound $La_{2-x}Sr_xCoO_4$ shows a similar insensitivity of the resistivity to Sr doping.[27] In the latter crystals,

insulating behavior with an activation energy of ~ 0.5 eV is observed for $0.4 \leqslant x \leqslant 0.7$, with a maximum resistivity for $x = 0.5$. The composition $x = 0.5$ in $La_{2-x}Sr_xCoO_4$ has equal numbers of Co^{2+} and Co^{3+} and therefore corresponds to our $\delta = 0.25$ samples.

IV. DISCUSSION

The important result of our annealing studies is that the removal of oxygen suppresses the AF order characteristic of the crystal with mostly Co^{3+}, while the peculiar ferromagnetic features, namely the size of the ferromagnetic peak in χ_a at T_N and the field induced ferromagnetic moment, are enhanced. In addition, the field dependent neutron scattering results provide strong evidence for magnetically distinct phases. The arguments are twofold. First, we have shown that the AF and FM peaks at high field have different correlation lengths along **c**. Second, the polarized neutron measurements show that both the AF and FM moments lie along **a** which is not possible in a single magnetic phase.

We propose that the simultaneous AF and FM peaks result from the existence of electronically distinct phases which exhibit distinct magnetic ordering. One phase has mostly Co^{3+} ions and is characterized by spins which are antiferromagnetically aligned along **a**, while the other phase has equal amounts of Co^{2+} and Co^{3+} which are FM aligned along **a**. Here, we will refer to the phase with mostly Co^{3+} as the AF phase and the phase with equal amounts of Co^{2+} and Co^{3+} as the FM phase.

The magnetization of $Bi_2Sr_2CoO_{6+\delta}$ evolves smoothly with decreasing δ to exhibit purely ferromagnetic behavior, suggesting that it is the removal of oxygen that increases the volume of the FM phase, which is Co^{2+} rich, while suppressing the AF ordering of the Co^{3+} spins in the AF phase. The decrease in the Néel transition temperature with decreasing δ likely results from finite inclusions of the FM phase in the AF phase.

We now discuss the microscopic mechanism for both antiferromagnetism and ferromagnetism in $Bi_2Sr_2CoO_{6+\delta}$. As discussed above, the spin state of Co^{3+} for the samples with δ near 0.5 is closest to S = 1, the intermediate spin state of trivalent Co. Co^{3+} at perfectly octahedral sites is usually found to have S = 0. However, a tetragonal distortion of the surrounding oxygen [Fig. 15(a)] favors the intermediate spin state of Co^{3+} because the crystal field energy splitting between the e_g and t_{2g} orbitals is lowered with respect to the electron–electron exchange. In $Bi_2Sr_2CoO_{6+\delta}$, the tetragonal distortion is (c–a)/a = (2.46–1.95)/1.95 = 0.26.[28] This should be compared to the nearly perfectly octahedral configuration in La_2CoO_4 or $LaCoO_3$ in which the S = 0 ground state may be preferred. For a sample in which every Co is in the 3+ state with S = 1, an AF interaction between neighboring Co^{3+} ions can be explained in the usual way by superexchange [Fig. 15(b)] between spins in the half filled z^2 and xy orbitals.[29]

We have shown that the volume of the ferromagnetic domains in $Bi_2Sr_2CoO_{6+\delta}$ increases with the removal of oxygen. Since the removal of oxygen is equivalent to electron doping, this suggests that it is the addition of Co^{2+} which
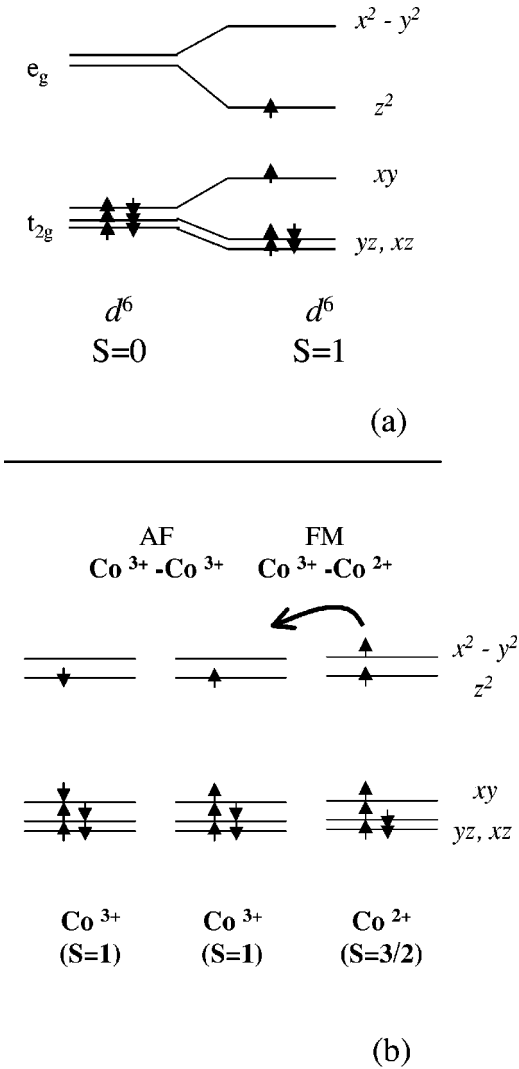
FIG. 15. (a) Crystal field splitting from the tetragonal distortion favors the intermediate spin (IS) state of Co^{3+}, which has unpaired spins in the xy and z^2 orbitals. (b) Expected magnetic interaction between neighboring Co^{3+} ions (left and center figures) in the AF phase ($\delta \simeq 0.5$) and adjacent Co^{3+} and Co^{2+} ions (center and right figures) in the FM ($\delta \simeq 0.25$) phase. The FM interaction can be explained by a double-exchange model in which delocalization of the electron is prevented by charge ordering.

induces the FM interaction. In addition, since the FM state seems most favorable when there are an equal number of Co^{3+} and Co^{2+} sites ($\delta = 0.25$), we infer that the FM interaction arises from nearest neighbor 3+ and 2+ sites. We have noted that our analysis of the susceptibility in the FM phase does not allow us to uniquely determine the spin state on the Co^{3+} and Co^{2+} sites. However, the data are consistent with either an equal mixture of Co^{3+} in the S = 1 state and Co^{2+} in the S = 3/2 state or an equal mixture of Co^{3+} in the S = 2 state and Co^{2+} in the S = 1/2 state. The former configuration seems most likely for several reasons. The first is that it preserves the local spin state of the Co^{3+} ion with doping. The second is that Co^{2+} is most commonly found in the high-spin, S = 3/2 state.[10] Last, as we show below, a FM interaction can be expected from this configuration. We

therefore discuss the ferromagnetic interaction occurring in the $\delta \sim 0.25$, FM phase in terms of nearest neighbor Co^{2+} and Co^{3+} ions which have S = 3/2 and S = 1, respectively.

The electron energy levels for the Co^{3+} in the S = 1 state and the Co^{2+} in the S = 3/2 state are indicated on the right-hand side of Fig. 15(b). This configuration is analogous to that of the manganites in which adjacent Mn^{4+} and Mn^{3+} have a FM interaction which is qualitatively explained by double-exchange (DE). The DE interaction favors the FM ground state because the delocalized spin, in this case, the spin in the $x^2 - y^2$ orbital, can satisfy the large on-site exchange (Hund's Rule) only if all sites have parallel spins. However, FM resulting from DE is usually associated with metallic behavior and canting in AF systems, while our FM samples are insulating and we do not observe a canting of the AF. Therefore, the simplest DE mechanism cannot explain the FM behavior. However, we believe that DE together with charge ordering of the Co^{2+} and Co^{3+} can explain our results. In particular, the charge-ordering will create a gap for exchange of Co^{3+} and Co^{2+} sites so that the $\delta \sim 0.25$ crystal will be insulating. As long as this gap is not too large, the nearest neighbor coupling will still be ferromagnetic.

We do not know why samples with δ intermediate between 0.25 and 0.5 are insulating. The constant activation energy, independent of δ, suggests that the conductivity may be limited by hopping of small polarons.

If the FM interaction in the FM phase arises from neighboring Co^{2+} and Co^{3+} ions, then we expect a checkerboard arrangement of the 3+ and 2+ ions as observed in $La_{1.5}Sr_{0.5}CoO_4$.[10] Such an in-plane charge ordering of Co^{2+} and Co^{3+} in $Bi_2Sr_2CoO_{6+\delta}$ should result in superlattice reflections detectable by neutron, x-ray or electron diffraction techniques. The neutron data in this regard are still incomplete. We have observed a peak in the neutron powder spectrum occurring at the position (0, 1, 2) or (1, 0, 2), which is consistent with a checkerboard of charge ordering and has an onset near 300 K. However, the peak is several orders of magnitude larger than expected for superlattice reflections resulting from a charge density wave and is only observed at a single reciprocal lattice vector. This will be studied with single crystals in the near future.

We note also that if the FM cluster contains a checkerboard of Co^{2+} and Co^{3+} spins, which do not have the same size moment then superlattice magnetic reflections should occur in the (0KL) plane at the positions (0, 1, L = even) or (0, 1, L = odd) as well as at (0, 0, L = even). We have not observed these peaks. However, they should be of order 25 times smaller than the FM peaks, assuming an equal mixture of S = 1 and S = 3/2 spins, and such weak scattering is difficult to detect. Clearly more structural and magnetic studies are required to unambiguously establish the charge-ordered checkerboard pattern.

We now consider a specific model of the spin arrangement in the phase-separated crystal that can help to explain the interaction of the two phases. In particular, any model must explain the simultaneous change in the AF and FM structure at H_c. Figure 16(a) shows a plausible magnetic ground state for adjacent AF and FM domains. In the figure, the boundary between the two phases occurs at the middle bc plane, since
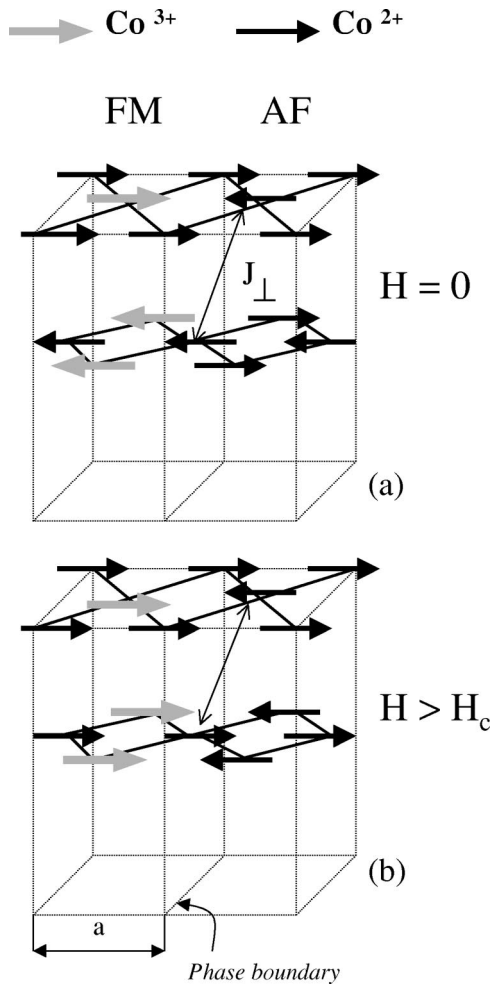
FIG. 16. Idealization of the two phase mixture. The left cell is in the $\delta = 0.25$ FM phase and the right cell is in the $\delta = 0.5$ AF phase. The zero field configuration is shown in (a). The double headed arrow connects nearest neighbor spins in adjacent layers in the AF phase, which are parallel at zero field. Note that in the $\delta \sim 0.25$ phase, the spins are ferromagnetically arranged in the layer, but at H = 0 adjacent layers point in opposite directions. The FM phase is pinned in each layer by the FM coupling, J_{FM}, between Co^{3+} and Co^{2+} spins at the phase boundary. (b) When the field is greater than H_c, every other layer (in both phases) rotates by 180°. The high field configuration preserves the in-plane interactions J_{FM} and J_{AF} but costs the perpendicular exchange $J_{\perp}^{AF}$ in the antiferromagnetic phase.

to the right of this plane all of the Co ions are 3+, while to the left, there are equal numbers of 2+ and 3+ Co ions. The AF phase consists of only Co^{3+} spins, which have the spin arrangement discussed in Sec. III A. Note that this means that all of the spins in a given ac plane point in the same direction, which is described by a ferromagnetic $J_{\perp}^{AF}$ between adjacent layers in the AF phase. The relevant in-plane exchange interactions are J_{FM} between nearest neighbor Co^{3+} and Co^{2+} spins and J_{AF} between nearest neighbor Co^{3+} spins. We assume that J_{FM} is less than J_{AF}.

In the top cobalt oxide layer shown in Fig. 16(a), the ordering of the AF spins at T_N creates an effective field pointing to the right on the FM cluster in this layer, which

therefore prefers to polarize in this direction. In the bottom layer, the AF ordering in the AF phase causes the FM cluster to polarize toward the left. In Fig. 16(a), all of the magnetic bonds are satisfied; all nearest neighbor Co^{3+} spins are antiparallel and all neighboring Co^{2+} and Co^{3+} spins are parallel. In addition, the perpendicular couplings between layers in the AF phase and between FM layers in the FM phase are satisfied because the FM clusters are antiparallel from layer to layer.

The model in Fig. 16 can explain the effect of the applied magnetic field, which induces both a change in the stacking between layers in the AF phase and the onset of an overt moment in the FM phase at the same field. Consider the interaction of the spins in the two-phase mixture in Fig. 16(a) with a magnetic field along the spin direction, **a**. The spins in the AF phase are not expected to contribute to the susceptibility since the field is applied along the easy axis of the AF. The field dependence of the $Co^{3+} - Co^{2+}$ FM phase should have the behavior shown in Fig. 5(c): a polarization of the moment along the field direction. However, in the mixed phase crystal, there is a strong in-plane FM exchange at the phase boundary which changes sign from layer to layer. The surrounding AF phase prevents the FM cluster from polarizing along the field direction without costing the in-plane FM exchange energy, J_{FM}, for those spins on the edge of the cluster.[30] However, a rotation of every other Co^{3+} AF layer allows the FM domain to polarize with the field, without breaking the in-plane bonds at the phase boundary [Fig. 16(b)]. Such a rotation results in a shift of the AF peaks from the positions (0, 1, L = even) to (0, 1, L = odd) at the same field as the onset in the uniform moment, as observed.

Although the model described in Fig. 16 can explain the behavior of a single FM domain in the AF host, the random direction of the FM domains makes the real system more complicated. Let us divide sites in each layer into A and B sublattices. The Co^{2+} in each FM domain may lie on the A or B sublattice. We call these A-type and B-type domains. Two such domains are shown in Fig. 17, separated by an AF region. We further assume that the stacking of the FM domains maintains the AB sublattice coherence, at least on a finite length scale. We see from Fig. 17 that the A-type and B-type domains are driven by the boundary with the AF to order in *opposite* directions. Thus in zero field the FM order is necessarily short range, with a coherence length of the order of the domain size. If we now apply a large magnetic field to the right along **a**, the spins in the B-type domain will flip. This will tend to flip the AF sublattice magnetization as explained earlier. However, this is opposed by the A-type domains, which do not flip and the orientation of the AF sublattice magnetization is then frustrated. This problem is reminiscent of the random field Ising model and, in fact, can be modeled as such.

Let us define M_S as the sublattice magnetization ($M_S = M_A - M_B$, where M_A and M_B are the magnetizations of the A-type and B-type domains, respectively). The coupling across the A-type and B-type FM domain walls can be modeled by an effective field $H_S(\mathbf{r})$, which is positive for A-type and negative for B-type domains. Extending the description to different layers, we see from Fig. 16(b) that for a given
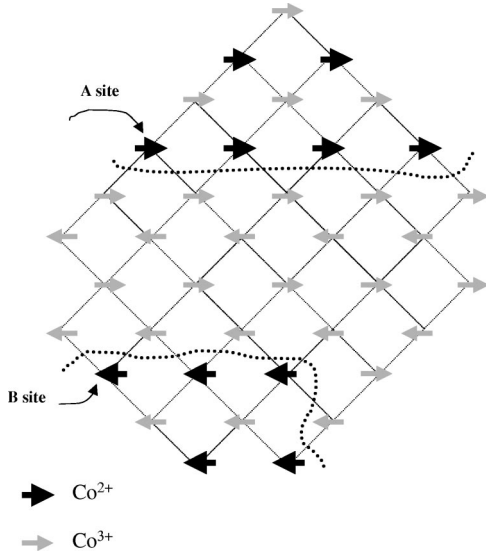
FIG. 17. Illustration of the zero external field spin configuration in a single layer, showing an AF region ($\delta=0.5$) in contact with two FM domains ($\delta=0.25$). The Co^{2+} spins lie on sublattice A in the top domain and on sublattice B in the bottom domain. Note the spin reversal of the FM domains.

FM patch, the coupling changes sign from one layer to the next. After coarse graining, we may write down the following effective Hamiltonian:

$$H_{eff} = \sum_j \int d^2 r (-1)^j H_S(\mathbf{r}) M_S(\mathbf{r}), \qquad (2)$$

where j is the layer index. The sum over j is restricted to the number of layers where the Co^{2+} coherently occupy A or B sites. Equation (2) is the classic random field Ising model. By the Imry–Ma argument, the system may break up into domains of size L, where the energy cost of the domain walls σL^{d-1} is balanced by the RMS fluctuation of the random field energy, which goes as $|H_S| L^{d/2}$. According to this argument, $d=2$ is the lower critical dimension; i.e., the system is always disordered below two dimensions. The physics for the two dimensional system is subtle, but fortunately we have a rigorous proof which states that the ground state is always disordered, independent of the strength of the random field.[31,32] Apparently, the system is always able to find a domain configuration which allows it to gain from the fluctuations in the random field configurations. The domain size will be extremely large for weak random fields, but nevertheless finite. Accepting this result, our picture is that in high magnetic field, the AF region will break up into large domains with opposite M_S. However, due to the $(-1)^j$ term in Eq. (2), the sublattice magnetization on neighboring layers is always opposite, i.e., the *relative* orientation of the sublattice is always flipped by applying a large magnetic field. This finally is the explanation of the field driven shift in the Bragg peaks [Fig. 9(b)] reported in this paper.

The random field model makes several predictions, which may be tested experimentally:

(1) In zero field, the c-axis correlation length of the FM Bragg peak is limited by the c-axis coherence of the sublattice occupation of the Co^{2+};

(2) In high field, the c-axis correlation length of the AF Bragg peak is limited by the same length as in (1);

(3) In zero field, the FM correlation length in the ab plane is limited by the domain size of the $\delta=0.25$ clusters;

(4) In high field, the AF correlation length in the ab plane is finite, but may be much larger than the FM correlation length in (3);

(5) The random field Ising model may explain the glassy behavior and hysteresis effects we observe.

The critical field for the transition described above is determined by a balance between the Zeeman energy gained by the spins in the FM domain and the cost in the exchange energy between layers in the AF domain. A simple calculation for a single FM patch in an AF background would give

$$H_c = \frac{z n_{AF}(J_\perp^{AF} S_{AF}^2)}{n_{FM}(g \mu_b S_{FM})}, \qquad (3)$$

where n_{FM} and n_{AF} are the densities of the FM and AF phases, respectively, $J_\perp^{AF}$ is the interlayer exchange in the AF phase, and $z=4$ is the number of nearest neighbors. The expression for H_c in (3) explains the decrease of H_c with T_{peak} shown in Fig. 12(b): a decreasing T_{peak} means the ratio of n_{FM} to n_{AF} is decreasing.

For the sample with $T_N=215$ K, the experimentally measured H_c is 1.6 T. We estimate δ close to 0.4 so that $n_{FM} = 2(1-2\delta)=0.4$. Using $S_{FM} \sim 5/4$ and $S_{AF} \sim 1$, the above equation gives $J_\perp \sim 38$ μeV.

It is important to point out that the spin arrangement in Fig. 16(a) assumes a specific three-dimensional charge stacking wherein all of the Co^{2+} ions are confined to the bc plane in the FM phase. Another configuration, in which all of the Co^{2+} ions are confined to the ac plane, would result in FM clusters in adjacent layers polarized in the same direction and a net moment at zero field which is not observed experimentally. Note that were the crystal tetragonal, the Coulomb interaction would be the same whether the Co^{2+} ions were confined to the bc or ac planes. The orthorhombic distortion and the fourfold modulation along a should lift this degeneracy. Confining the Co^{2+} in the FM phase to the bc plane is necessary to explain the observation of antiparallel adjacent FM layers.

Since the T_c for the FM phase is of order 100 K, we argue that when T_N is greater than $T_c \sim 100$ K, the FM clusters order because of the effective field imposed at the phase boundary with the long range ordered AF phase. On the other hand, the three-dimensional charge ordering of the Co^{2+} and Co^{3+} shown in Fig. 16(a) must exist above or at the transition to 3D AF order, so that the FM layers polarize in opposite directions from layer to layer. Since we ascribe the FM peak and Curie tail in the susceptibility to the magnetic fluctuations in the FM phase, the in-plane charge ordering must occur at temperatures well above T_N. Note that the suppression of the susceptibility at the Néel transition is explained by the pinning of the FM domains when the AF phase orders.

The above model does not address the mechanism which prefers the charge segregation necessary to create the Co^{2+} rich FM clusters. Recent TGA measurements suggest that annealing at temperatures as high as 900 °C is necessary to obtain the phase separation.[24] We have also noted that the FM Curie tail in the susceptibility, which is a measure of the amount of FM phase, extends up to 400 K. Therefore, we do not believe that phase separation is driven by a competition between FM and AF interactions. Rather, the distinct magnetic regions appear to result from two electronically distinct phases which exist at higher temperatures (>400 K) than the magnetic order. In the similar cobalt–oxide system, $La_{2-x}Sr_xCoO_4$, charge ordering in the $x=0.5$ crystal occurs near 700–800 K, while the magnetic ordering occurs at 30 K.[10] $La_{1.5}Sr_{0.5}CoO_4$ is, of course, optimized for charge ordering of the Co^{2+} and Co^{3+} ions and does not require any large-scale segregation of charge. In $Bi_2Sr_2CoO_{6+\delta}$, phase separation into regions which are Co^{2+} rich and regions which are Co^{2+} poor is energetically unfavorable because the resulting long range Coulomb energy is expected to be large. For small electron densities (i.e., small deviations from $\delta=0.5$), the charge segregation energy can be of order 1 eV per charge. However, if the oxygen vacancies can move with the added electrons, the charge assembly energy can be considerably reduced. Since the oxygen is likely mobile over the range of temperatures where the annealing is effective, we believe that the FM and AF phases are actually *chemically*

distinct $\delta=0.25$ (FM) and $\delta=0.5$ (AF) phases. We note that the neutron scattering measurements thus far do not show any evidence of chemical phase segregation due to inhomogeneous oxygen doping. For example, we are not able to resolve two c-axis lattice constants which might be expected for coexisting oxygen-rich and oxygen-poor phases. X-ray and electron diffraction measurements are in progress to look for both charge ordering and oxygen phase separation.[24,33]

V. CONCLUSION

This is the first extensive study of the origin of the ferromagnetism in $Bi_2Sr_2CoO_{6+\delta}$. We have shown that the oxygen rich crystal with δ close to 0.5 is an antiferromagnet of Co^{3+} spins while the crystal with $\delta \simeq 0.25$ is predominantly ferromagnetic. At intermediate oxygen content, the crystal appears to contain phase separated regions of the hole rich, AF and hole poor, FM phases. We have constructed a model of interacting domains to account for the similar ordering temperature and field dependence of the AF and FM phases in the two-phase system.

[1] E. Dagotto, T. Hotta, and A. Moreo, Phys. Rep. **344**, 1 (2001).

[2] M.B. Salamon and M. Jaime, Rev. Mod. Phys. **73**, 583 (2001).

[3] A.P. Ramirez, J. Phys.: Condens. Matter **9**, 8171 (1997).

[4] M. Abbate, J.C. Fuggle, A. Fujimori, L.H. Tjeng, C.T. Chen, R. Potze, G.A. Sawatzky, H. Eisaki, and S. Uchida, Phys. Rev. B **47**, 16124 (1993).

[5] H.-W. Hsu, Y.-H. Chang, and G.-J. Chen, Jpn. J. Appl. Phys., Part 1 **39**, 61 (2000).

[6] D. Akahoshi and Y. Ueda, J. Solid State Chem. **156**, 355 (2001).

[7] G. Briceño, H. Chang, X. Sun, P.G. Schultz, and X.-D. Ziang, Science **270**, 273 (1995).

[8] C. Martin, A. Maignan, D. Pelloquin, N. Nguyen, and B. Raveau, Appl. Phys. Lett. **71**, 1421 (1997).

[9] T. Vogt, P.M. Woodward, P. Karen, B.A. Hunter, P. Henning, and A.R. Moodenbaugh, Phys. Rev. Lett. **84**, 2969 (2000).

[10] I.A. Zaliznyak, J.P. Hill, J.M. Tranquada, R. Erwin, and Y. Moritomo, Phys. Rev. Lett. **85**, 4353 (2000).

[11] A. Moreo, S. Yunoki, and E. Dagotto, Science **283**, 2034 (1999).

[12] J. Mira, J. Rivas, G. Baio, G. Barucca, R. Caciuffo, D. Rinaldi, D. Fiorani, and M.A. Señarís Rodríguez, J. Appl. Phys. **89**, 5606 (2001).

[13] R. Caciuffo, D. Rinaldi, G. Barucca, J. Mira, J. Rivas, M.A. Señarís Rodríguez, P.G. Radaelli, D. Fiorani, and J.B. Goodenough, Phys. Rev. B **59**, 1068 (1999).

[14] M.A. Señarís-Rodríguez and J.B. Goodenough, J. Solid State Chem. **118**, 323 (1995).

[15] J.M. Tarascon, P.F. Miceli, P. Barboux, D.M. Hwang, G.W. Hull, M. Giroud, L.H. Greene, Y. LePage, W.R. McKinnon, E. Tsel-

epis, G. Pleizier, M. Eibschutz, D.A. Neumann, and J.J. Rhyne, Phys. Rev. B **39**, 11587 (1989).

[16] The authors of Ref. 15 determined the spin direction using powder samples. Since $Bi_2Sr_2CoO_{6+\delta}$ is nearly tetragonal, it is difficult to distinguish a from b in a powder measurement.

[17] Throughout this paper we use the formal oxidation state to differentiate samples. However, we understand that the positive charge may reside at least in part on the oxygen ions as it does in the copper oxides.

[18] M.V. Zinkevich, S.A. Prodan, Y.G. Zonov, and V.V. Zashook, J. Solid State Chem. **136**, 1 (1998).

[19] Since orthorhombic a is slightly shorter than b, the effective interplane interaction is said to be FM if spins in the same ac plane point in the same direction.

[20] We assume a spherically symmetric charge distribution to calculate F (Q). *International Tables for Crystallography*, edited by A. J. C. Wilson (Kluwer Academic, Dordrecht, 1995), Vol. C.

[21] M. Greven, R.J. Birgeneau, Y. Endoh, M.A. Kastner, M. Matsuda, and G. Shirane, Z. Phys. B: Condens. Matter **96**, 465 (1995).

[22] R.J. Birgeneau, J. Skalyo, Jr., and G. Shirane, Phys. Rev. B **3**, 1736 (1971).

[23] R.J. Birgeneau, J. Als-Nielsen, and G. Shirane, Phys. Rev. B **16**, 280 (1977).

[24] K. Thomas (unpublished).

[25] T. Thio, T.R. Thurston, N.W. Preyer, P.J. Picone, M.A. Kastner, H.P. Jenssen, D.R. Gabbe, C.Y. Chen, R.J. Birgeneau, and A. Aharony, Phys. Rev. B **38**, 905 (1988).

[26] This lower limit is determined for the case where the staggered

moment lies along b, for which $\sin^2(\alpha)=0.05$. If the staggered moment is, instead, along c, $\sin^2(\alpha)=0.95$ and the ratio of SF to NSF scattering will approach 32:1 at the (0, 1, 1) reflection.

[27] Y. Moritomo, K. Higashi, K. Matsuda, and A. Nakamura, Phys. Rev. B **55**, R14725 (1997).

[28] The tetragonal distortion is calculated using the average in-plane and out-of-plane Co–O bond length. The local distortion varies over the 4 unique positions in the superstructure.

[29] J. Kanamori, J. Phys. Chem. Solids **10**, 87 (1959); J.B. Goodenough, Phys. Rev. **100**, 564 (1955).

[30] This argument assumes that the total in-plane exchange energy at the boundary is greater than the Zeeman energy of the spins in the cluster. This depends not only on the magnitude of J_{FM} compared to $g\mu_b S_{FM} H$, but the number of spins at the boundary compared to the number of spins in the cluster.

[31] J.Z. Imbrie, Phys. Rev. Lett. **53**, 1747 (1984).

[32] M. Aizenman and J. Wehr, Phys. Rev. Lett. **62**, 2503 (1989); for a review, see D. P. Belanger in *Spin Glass and Random Fields*, edited by A. P. Young (World Scientific, Singapore, 1998).

[33] H. Zandbergen (unpublished).